Kerstin Absenger, Bsc

Coherent Nuclear Wave Packet Dynamics of Aluminum Dimers inside Superfluid Helium Nanodroplets

Master's Thesis

to achieve the university degree of
Diplom-Ingenieurin

Master' degree programme:
Technical Physics

submitted to

Graz University of Technology

Supervisor

Assoc. Prof. Dipl.-Ing. Dr.techn. Markus Koch

Institut für Experimentalphysik, TU Graz

Graz, 08.02.2021

EIDESSTATTLICHE ERKLÄRUNG

Ich erkläre an Eides statt, dass ich die vorliegende Arbeit selbstständig verfasst, andere als die angegebenen Quellen/Hilfsmittel nicht benutzt, und die den benutzten Quellen wörtlich und inhaltlich entnommenen Stellen als solche kenntlich gemacht habe.

I declare that I have authored this thesis independently, that I have not used other than the declared sources/resources, and that I have explicitly marked all material which has been quoted either literally or by content from the used sources.

———————————————————   ———————————————————
Datum/Date   Unterschrift/Signature

Abstract

Time-resolved photoelectron spectroscopy is a powerful method for the investigation of dynamical electronic and nuclear processes in isolated molecules and clusters on a femtosecond timescale. Within this master thesis, aluminium dimeres localized inside helium nanodroplets (He_N) have been investigated with femtosecond spectroscopy to observe coherent molecular dynamics. Vibrational wave packet oscillations were observed, that disperse and eventually rephase and form revivals of this oscillations.

Within 50 and 200 ps after photoexcitation, 90 percent of the aluminium dimeres are ejected from the He_N. The presencs of the helium environment and additional dopants can lead to dissipation and decoherence, observable in the revival oscillations. This work builds on the first demonstration of coherent molecular dynamics in He_N with indium dimeres (B.Thaler et al., Physical Review Letters 124(11):115301, 2020). Although new insides to photoinduced dynamics could be obtained, the long revival times of indium dimere molecular dynamics made the observation of the influence of additional dopants not possible. The next step in the research project was to find a molecule with revival periods that are short enough for the continuous observation of the molecular dynamics. By the excitation of aluminium dimeres a molecular state was found that shows molecular dynamics with $1/10^{th}$ of the revival period of indium, what fulfills the requirements for a continues observation of the wave packet oscillations.

Analysis of the coherent wave packet signal in the time domain and in the frequency domain, for which sliding window Fourier transformation was used, show ongoing wave packet oscillations up to 200 ps. With (3.89 ± 0.02) eV pulse energy a revival period of (31.4 ± 0.2) ps with a revival duration of (3.5 ± 0.3) ps and a mean oscillation frequency of (5.81 ± 0.02) THz was measured. The dispersion time, revival period and oscillation frequencies can be assigned to the electronically excited E-state of the aluminium dimer with very good agreement. A further indicator for an oscillation of the He_N after excitation, what has already been postulated in former work with indium, has been found by the observation of the frequencies and amplitudes at different revival times.

Due to its high reactivity and high evaporation temperature, the investigation of aluminium required the reconstruction of the pickup facilities. A new crucible setup and current source were built.

The next steps in this project will lead to the development of a microsolvation setup for a better understanding of the bridging from the molecular processes in gas phase to the molecular structure in solution. Although aluminium has difficult operation conditions, its high-frequent molecular dynamics make it a promising candidate for microsolvation.

Zusammenfassung

Zeitaufgelöste Photoelektronenspektroskopie bietet die Möglichkeit Dynamiken von elektronischen und atomaren Prozessen in isolierten Molekülen und Clustern auf Femtosekunden-Zeitskalen zu untersuchen. Innerhalb dieser Masterarbeit wurden die koherenten Moleküldynamiken von Aluminiumdimeren in Heliumtropfen (He_N) untersucht. Vibrationswellenpackete, die zerfließen und sich in Form von Revivals wieder reformieren, konnten beobachtet werden. Innerhalb von 50 bis 200 ps nach Photoanregung, wurden 90 Prozent der Aluminiumdimere aus dem He_N ausgestoßen. Die Heliumumgebung und weitere Dotieratome können zu Dissipation und Dekohärenz führen, was im Revivalsignal beobachtbar ist. Diese Arbeit baut auf die ersten Demonstrationen von koherenten Moleküldynamiken von Indiummolekülen in He_N auf (B.Thaler et al., Physical Review Letters 124(11):115301, 2020). Obwohl neue Einblicke in photoinduzierte Dynamiken gemacht wurden, verhinderten lange Revivalzeiten die Untersuchung des Einflusses weiterer Dotieratomen. Ein Molekül mit ausreichend kurzen Revivalzeiten zu finden, um den Abfall der Dynamik mit zunehmender Dotierung zu beobachten, war ein nächster wichtiger Schritt des Projekts. Im Aluminiumdimer konnte ein angeregter Zustand gefunden werden, der Moleküldynamiken mit $1/10^{tel}$ der Revivalzeit von Indium besitzt und damit diese Anforderungen erfüllt.

Die Untersuchung des koherenten Wellenpacketsignals in der Zeit- und Frequenzdomäne, für die Sliding Window Fourier Transformation benutzt wurde, zeigt Wellenpacketoszillationen bis 200 ps. Mit (3.89 ± 0.02) eV Pulsenergie konnten Revivalperioden von (31.4 ± 0.2) ps mit einer Revivaldauer von (3.5 ± 0.3) ps und einer mittleren Oszillationsfrequenz von (5.81 ± 0.02) THz beobachtet werden. Die Dispersionszeit, Revivalperiode und Oszillationsfrequenz konnten mit sehr guter Übereinstimmung dem elektronisch angeregten E-Zustand zugewiesen werden. Beobachtungen der Frequenzen und Amplituden von unterschiedlichen Revivals ergaben einen weiteren Indikator für eine Oszillation des He_N nach der Photoanregung, die bereits in der vorangehenden Arbeit mit Indium beobachtet wurde.

Aufgrund der hohen Reaktivität und hohen Verdampfungstemperatur forderte die Untersuchung von Aluminium Änderungen der Pickup-Anlage und neue Heizöfen und eine neue Stromquelle wurden installiert.

In den nächsten Schritten des Projekts wird ein Mikrosolvation-Setup zur Untersuchung des Übergangs von molekularen Prozessen in Gasphase zu molekularen Prozessen in Lösung stattfinden. Obwohl Aluminium schwierige Betriebsbedingungen liefert, ist es durch seine kurzen Revivalzeiten ein sehr vielversprechendes Element für Mikrosolvation.

Contents

1 Introduction

1.1 Project Goal

Within the project "Photoinduced Dynamics in a Quantum Fluid Environment" the use of helium nanodroplets (He_N) for time-resolved spectroscopy is investigated. The effects on the coherent nuclear motion and on electronic structure is studied. He_N, which provide a favourable environment in this scope of application [1] [2], have also been observed to distort potential energy curves (PECs). Experiments with LiI [3] lead to intramolecular relaxations, what spoke against the use of He_N as containers for time-resolved spectroscopy at first. Experiments on He_N doped with indium (In) and indium dimers (In_2), what have been conducted in our research group within the last years, offered the observation of long-lasting wave packet (WP) dynamics [4], making He_N favourable containers for time-resolved spectroscopy [5]. New insights into photoinduced dynamics with less than 100 fs temporal and less than 10 meV energetic resolution were revealed. For example, in the In–He_N system, part of the excited state electronic energy leads to expansion of the solvation shell within 600 fs, initiating a collective shell oscillation with a period of about 30 ps [6]. Also the expansion of the solvation shell and dopant ejection from the droplet after photoexcitation of indium dimers was observed [7].

These results were obtained in some of the first studies done on molecular dynamics inside He_N in a time domain that is relevant in processes like photosynthesis and photovoltaics. Currently, many interesting ultrafast molecular dynamics are not observable yet. Future steps in this research project should lead to microsolvation environments inside He_N. That would allow to produce a solvation shell, in which the number and species of solvent molecules can be controlled and the observation of chemical reactions, while changing from a low pertubing He_N environment to a real-world environment, would be made possible. A controlled microsolvation environment could be generated, for example, by loading He_N droplets with one Al_2 molecule and subsequently adding species such as H_2O molecules or Ar atoms as mediators. Thereby the coupling to internal droplet excitations can be increased by adding intermediate vibrational modes. The mediator species will influence the PE transient time scans as the wave packet oscillations decay faster. A combination with different noble gas atoms, as well as polar and non-polar classical solvents (H_2O, C_6H_{14},...) can provide insight into the dependence of WP dephasing and energy dissipation on mass, polarizability, dipole moment or vibrational modes of the mediator species. The active control of decoherence and energy dissipation by establishing a microsolvation can improve ultrafast experiments inside He_N. Adjusting the molecule-bath energy transfer rate to an optimum level might enable a series of previously impossible investigations by lowering the perturbation of coherent nuclear dynamics. Steadily growing microsolvation environments may allow a bridging from gas phase to solution and thereby trace the external influence on molecular

dynamics from the He environment to a real-world solvent [8].

With In_2 it was already possible to observe and account processes like the solvation shell expansion, wave packet oscillations and dopant ejection. Due to long revival times, that prohibited the observation of the influence from other dopants, and a lack of literature and calculated potentials for In_2, a new specimen had to be chosen for further experimentation. Within the work for this master thesis experiments have been performed on aluminium dimers, that have a very similar electronic structure to In_2 but have a lower mass and are a simpler system. Aluminium dimers are better studied and with the Morse parameters known, the interpretation of PE spectra and assignments to states is easier. Higher vibrational frequencies should also increase the mismatch to He internal modes and thereby enable the decreasing of energy dissipation.

1.2   Electronic and Vibrational States of Diatomic Molecules

The excitation energy E of a molecule can be seen, in good approximation, as the sum of the rotational, vibrational and electronic excitation:

$$E = E_{\mathrm{rot}} + E_{\mathrm{vib}} + E_{\mathrm{el}} \tag{1}$$

Figure 1 shows the vibrational (quantum number v) and rotational states (quantum number J) of two electronic states. The arrows show possible transitions between the states. Ro-vibronic transitions, that are the simultaneous change of rotational, vibrational and electronic states, have energies in the UV up to the visible spectrum. Ro-vibrational transitions are in the infrared spectrum and rotational transitions have energies in the meV-range [9].

1.2.1   Morse Potential and Vibrational Eigenstates

To describe the potential energy of the state of a diatomic molecule, the Morse Potential is a well established model [9]. The formula for the Morse potential is determined by three parameters: the equilibrium internuclear distance r_{e}, the dissociation energy D_{e} and the fundamental frequency ω_{e}:

$$V(r) = D_{\mathrm{e}}(1 - e^{-\beta(\mathrm{r}\text{-}\mathrm{r_e})})^2 \tag{2}$$

with $\beta = \omega_{\mathrm{e}}\sqrt{\frac{\mu}{2D_{\mathrm{e}}}}$ and μ as the reduced mass of the molecule. As depicted in figure 1, within each electronic energy state there are many vibrational energy states. The eigenvalues of these vibrational states can be calculated with:

$$E_{\mathrm{v}} = \hbar\omega_{\mathrm{e}}(v + 1/2) - \frac{[\hbar\omega_{\mathrm{e}}(v + 1/2)]^2}{4D_{\mathrm{e}}} \tag{3}$$
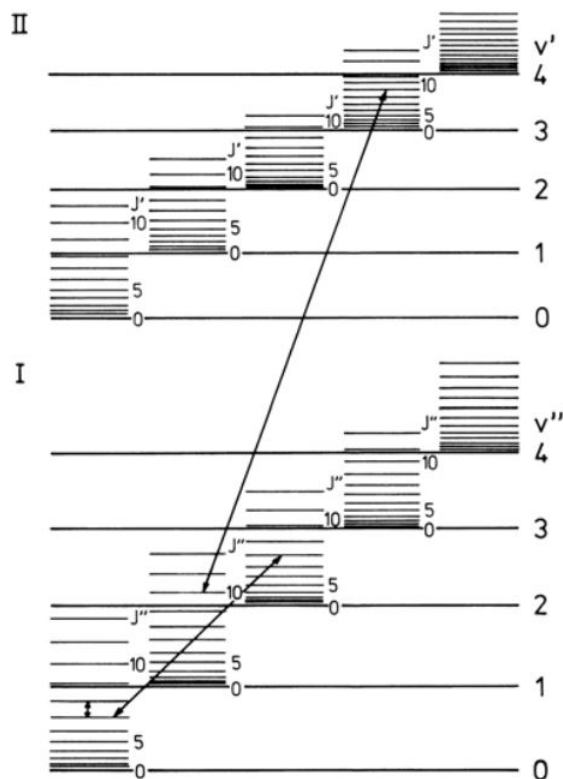
Figure 1: Vibrational (quantum number v) and rotational states (quantum number J) of two electronic states. The arrows show possible transitions between the states. [9]

.

wherein the first term yields the equidistant energy values derived from the model of a harmonic oscillator and the second term considers the anharmonicity of the Morse potential. The anharmonicity leads to the decreasing distance between the energy levels for higher v. When looking at wave packets, that can be formed out of several vibrational states, what will be done in section 1.3, one can see that the revival times of the wave packets are depending on the energetic difference between the lowest and highest state pair distances that are contributing to a wave packet.

1.2.2 Molecular Term Symbol

For molecules with several valence electrons, like aluminium dimers that have two electrons beyond a filled shell configuration, the coupling of molecular orbitals has to be taken into account for the characterization of the overall state. The full characterization of a state is also

important since in electric dipole transitions selection rules limit the transitions that are possible and thereby constrain the amount of excitable states from a certain ground state. For that, the term symbol is used as an abbreviated description of a multi-electron atom or molecule [10]. For the projection onto the molecular axis of the orbital angular moment L_z, the following condition applies:

$$L_z = \pm \Lambda\hbar, \ \Lambda = |\Sigma\lambda_i| \tag{4}$$

The outer electrons contribute to L_z each by $\lambda_i = 0,1,2,...$, which is the multi-electron equivalent to $|m_l|$ that is denoted with $\sigma, \pi, \delta, ...$ as single electron molecular orbitals. A given electron configuration for multi-electron molecules is denoted with the symbols:

$$\Lambda = \Sigma, \ \Pi, \ \Delta, ... \tag{5}$$

for the values 0,1,2, ... following the denotation of single-electron states. Also the spins of the electrons have to be taken into account. They couple to an overall spin S with the quantum number $S = \sum m_{S_i}$. To consider the projection of the spins of the electrons on the principal axis (inconveniently) also the sign Σ has been chosen:

$$\Sigma = S, S - 1... - S \tag{6}$$

If the electronic orbital angular momentum L and the electronic spin angular momentum S lie in the molecular axis, the sum of their projection is the total angular momentum $\Omega = |\Lambda + \Sigma|$, what is called Hund's case a. If the electronic orbital angular momentum L and the electronic spin angular momentum S lie not in the molecular axis $\Omega \leq |\Lambda + \Sigma|$ applies, the spin-orbit coupling is weak or non-existent and we have Hund's case b. Hund's case a gives a simple precession motion. The quantum numbers of a molecule wave function can for this case be summed up in the term symbol as $^{2S+1}\Lambda_\Omega$. Hund' case b is the case for light atoms, where the mutual Coulomb forces are stronger than the spin-orbit coupling and the electronic spin angular momentum vector is not coupled to the molecular axis. In this case the molecule performs a more complicated motion of the combined precession motions [11]. For Hund's case a, all molecular orbitals, except the $\Lambda = 0$ state, are two-fold degenerated. For Hund's case b this is not the case.

Every state also has two states of parity. For a configuration with an $L_z = 0$ this would be written as Σ_g and Σ_u for even and odd respectively. The term symbol also considers if the wave function is symmetric or anti-symmetric regarding the mirroring around the principal axis of the molecule. Σ^+ and Σ^- mean symmetric or anti-symmetric respectively. Figure 2 shows a table with the possible molecular states of Al_2 and from which atomic states they arise. The term symbols specify the parity and symmetry of each excited state and thereby limit the possibilities of transitions since the parity has to change within each transition.

Separated atom limit	Molecular States[b]
$s^2p,^2P^0 + s^2p,^2P^0$	$X\,^3\Pi_u$, $A\,^3\Sigma_g^-$, $1^3\Pi_g$, $^3\Delta_u$, $^3\Sigma_u^+(2)$, $^1\Sigma_g^+(2)$, $^1\Sigma_u^-$, $^1\Pi_g$, $^1\Pi_u$, $^1\Delta_g$
$s^2p,^2P^0 + s^2s,^2S$	$2^3\Pi_g$, $^3\Pi_u$, $^3\Sigma_g^+$, $^3\Sigma_u^+$ $^1\Sigma_g^+$, $^1\Sigma_u^+$, $^1\Pi_g$, $^1\Pi_u$
$s^2p,^2P^0 + sp^2,^4P$	$^5\Sigma_g^+$, $^5\Sigma_u^+$, $^5\Sigma_g^-(2)$, $^5\Sigma_u^-(2)$, $^5\Pi_g(2)$, $^5\Pi_u(2)$, $^5\Delta_g$, $^5\Delta_u$, $E\,^3\Sigma_g^-$, $F\,^3\Sigma_g^-$, $E'\,^3\Pi_g$, $G\,^3\Pi_g$, $B\,^3\Sigma_u^-$, $^3\Sigma_u^-$, $^3\Sigma_g^+$, $^3\Sigma_u^+$, $^3\Pi_u(2)$, $^3\Delta_g$, $^3\Delta_u$

Figure 2: Table of molecular states of Al_2 and their separated atom limit [12]
.

1.2.3 Potential energy curves of Al_2 and Al_2^+ States

The PECs of the states of Al_2, that have been shown in figure 2 and are dipole connected to the Al_2 $X^3\Pi_u$ ground-state, are visible in figure 3 [12]. Figure 4 shows a plot of all ionisable Al_2^+ states [13]. Their transition energies from the ground state are listed in table 3 in section 3.1.4, where the assignment of the measured parameters to the E-state will be done and the reachable ionic states will be discussed. From the even states only odd states should be accessible and thereby the lowest accessible ionic state should be the $A^2\Pi_u$ state.

1.2.4 Excited States of Al_2

To decide which excited states, that have been observed to be stable in other experiments [12], fit to our observations, a short description of the excited states of Al_2 will be done in the following.

The band systems E, E", F' and F show multiplet splittings. The states E', F", G, H and H' show only single vibrational features. Figure 5 shows the E-X and E'-X band system [12]. The band systems E, E", F' and F should conform to Hund's case b. Thereby the electrons are mainly influenced by their mutual coulomb repulsion and barely by the spins. The total wave function is thereby in good approximation a product of the position wave function of all electrons and the spin wave function of all electrons and should have very small multiplet splittings. While the multiplet splittings of this states should not be observable, all the measured bands show multiplet splittings with the same range. This has to correspond to a multiplet splitting of the ground state of Al_2. Thus the Al_2 ground state is split into components with term energies of 0.0, 30.4, and 63.4 cm^{-1}.

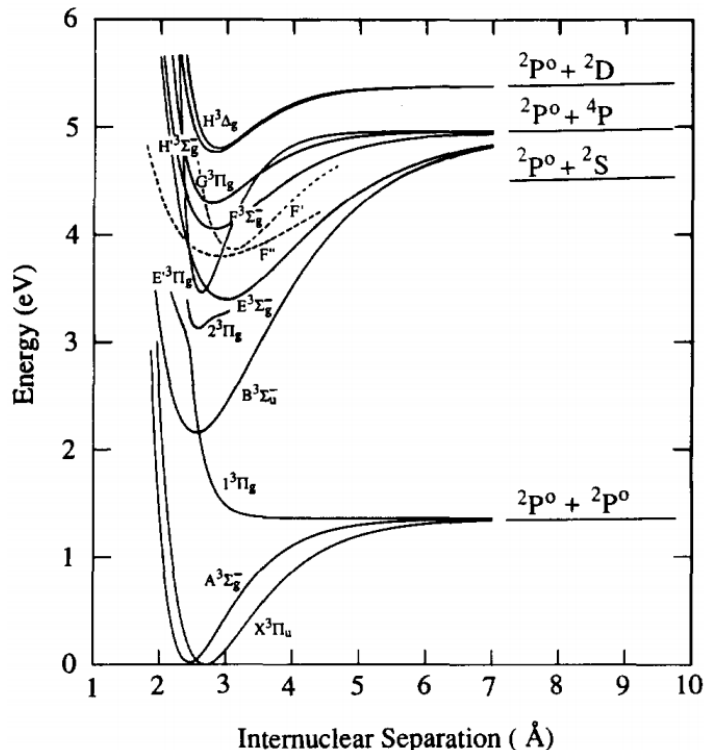The states E',F",G , H and H' of the apparent singlet bands are most likely to belong to Hund's case a.

Figure 3: Schematic potential energy curves for the electronic states of Al_2. The potential curves are drawn using the parameters given in reference [12]
.

We can assume that the states that show the multiplet splittings and the states with the singlet bands are not excitable from the same ground state.

The $E'^3\Pi_g \leftarrow X^3\Pi_u$ transition is the most intense band of Al_2 in any spectral region. Though it has been shown that non-adiabatic coupling leads to a very fast dissociation, with Al_2 ultimately falling apart through the repulsive $1^3\Pi_g$ state. Although the $E \leftarrow X$ transition is way weaker than the $E' \leftarrow X$ transition, the large change of bond length in the electronic excitation $2^3E\Sigma_g \leftarrow X^3\Pi_u$ should make a long vibrational progression possible if no other relaxation occurs, what would be very favorable for the investigation of microsolvation [12]. The E-band is ranging from 366.4 nm to 344.9 nm. It is also possible to combine the bands of the E-state and E"-state into a single band system. By including the E"-state, the state would range from 366.7 down to 327.6 nm in gas phase. The F"-band is quite irregular. The intensity of the F'-band system is quite low compared to other band systems, and above 32 500 cm^{-1} this system is obscured by the much more intense $F \leftarrow X^3\Pi_u$ band.
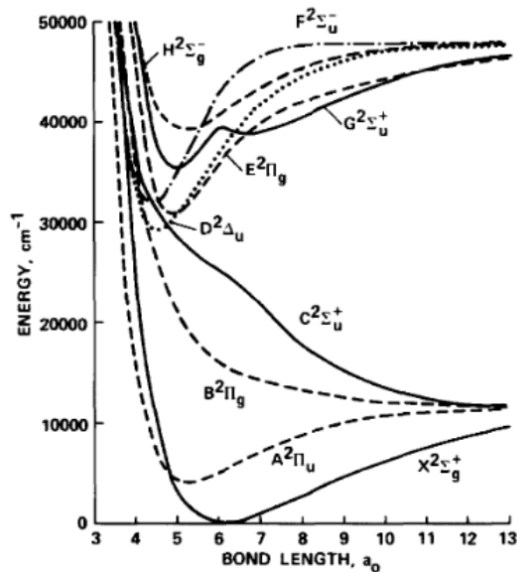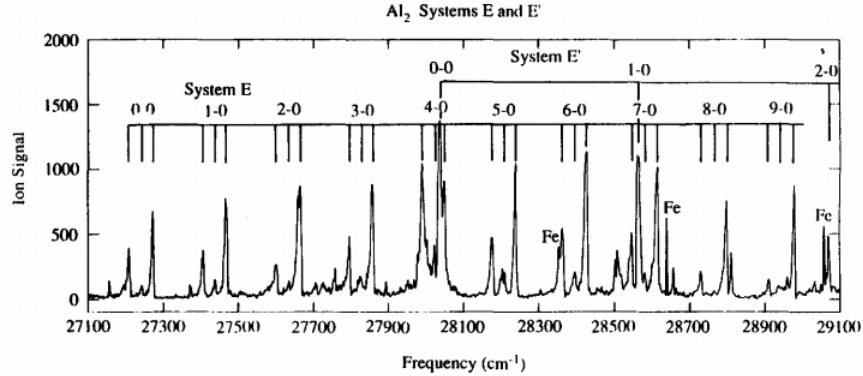
Figure 4: Potential energy curves of the low lying Al_2^+ states [13] - 1 a_0 = 0.53 Å

The F-band is, like the E-band, red-degraded, but the vibrational progression is not nearly as extensive as observed after the $E^3\Pi_g \leftarrow X^3\Pi_u$ transition. The bond length of the F-state lies between that of the ground state (2.701 A) and that of the $E^3\Pi_g$-state (2.99 A). The only dipole-allowed transition from the F state is to the repulsive $B^2\Pi_g$ state, what would speak for the possibility of a long vibrational progression though [13]. The H'-state and it's rotational states are not well described by the standard model and strongly perturbed [12].

In conclusion, the E-band is theoretically the most prominent band for our experiment since it is expected to offer a stable long lasting dynamic.

1.3 Creation of Wave Packets in the Electronically Excited State

When diatomic molecules are vibronically excited and the bandwidth of the pulse is broad enough, the coherent superposition of different vibrational levels leads to the formation of a wave-packet (WP), which evolves and propagates along the excited state molecular potential [9]. Initially, molecules are in there electronic and vibrational ground states. Figure 6 shows a schematic representation of a WP excitation. For simplicity there is just one excited wavefunction drawn, although the excited state is a superposition of several vibrational states in the potential energy curve.

Figure 5: The E-X and E'-X band systems of Al_2 from reference [12]

In the classical picture, the electron probability densities have their maxima at the outer turning points of the potential energy curve (PEC) for all excited states, except the ground state which has its maximum in its center. The Franck-Condon (FC) principle uses this picture and states, that the absorption from the ground state in a higher lying state is the strongest for states, that have their wave function maximum, hence there turning points, at the same radial distance as the ground state wave function maximum. The radial distance in which the transition probability is especially high is called a Franck-Condon window [9].

1.4 Temporal Evolution of a Vibrational Wave Packet

To describe the temporal evolution of a wave packet, the time dependent Schroedinger equation is used:

$$H\left|\Psi_{\mathrm{n}}(t)\right\rangle = E_{\mathrm{n}}\left|\Psi_{\mathrm{n}}(t)\right\rangle = i\hbar\frac{\delta\left|\Psi_{\mathrm{n}}(t)\right\rangle}{\delta t} \tag{7}$$

If a state that is not an eigenstate, like in the case of a wave packet, which is the superimposition of vibrational states, it can be written as a superposition of eigenstates. Amplitudes can be used to consider the amount of contribution of each state to the overall state. To reduce computational effort, the states can be made time independent by conflating the time dependence, transition probability and phase within the weight factors:

$$\left|\Psi(t)\right\rangle = \sum_{n} a_{\mathrm{n}}e^{-\mathrm{i}\Phi(t)}\left|\Psi(t)\right\rangle = \sum_{n} a_{\mathrm{n}}(t)\left|\Psi(t)\right\rangle \tag{8}$$

To consider the higher transition probabilities for radial overlapping maxima of molecular state functions, the Franck-Condon factors have to be calculated as weight factors. Therefor the spacial overlap of the respective initial and final state is calculated, whereby the Born-
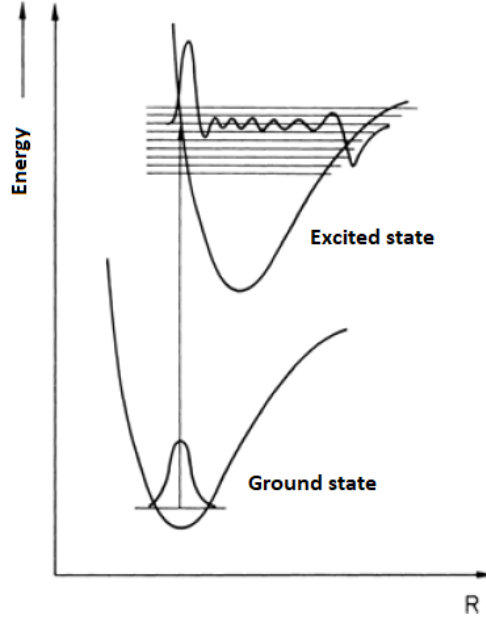
Figure 6: Photoexcitation from the ground state into an excited state. For simplicity there is just one excited wavefunction drawn, although the excited state is a superposition of several vibrational states in the potential energy curve. (Figure addapted from [9])

Oppenheimer principle is considered:

$$a_{\text{FC}} = \int \Psi_{\text{i}}{}^{*}\Psi_{\text{f}} dr \tag{9}$$

Here $\Psi_{\text{i}}{}^{*}$ and Ψ_{f} represent the initial and final state. To investigate the temporal evolution of the WP, the expectation value of the position operator can be calculated like this:

$$X_{\text{mn}} = \langle \Psi_{\text{m}} | \hat{X} | \Psi_{\text{n}} \rangle \tag{10}$$

$$< X(t) >= \sum_{m,n} a^{*}{}_{\text{m}}(t) X_{\text{mn}} a_{\text{n}}(t) \tag{11}$$

The time evolution of the expectation value of the position operator of a diatomic molecule is shown in figure 7 [14].

In figure 7 it is shown, that the expectation value for some times shows an oscillating motion, like visible in the inset, disperses after some time and forms again at the revival times. This molecular dynamic takes place on femto- to picosecond timescales.
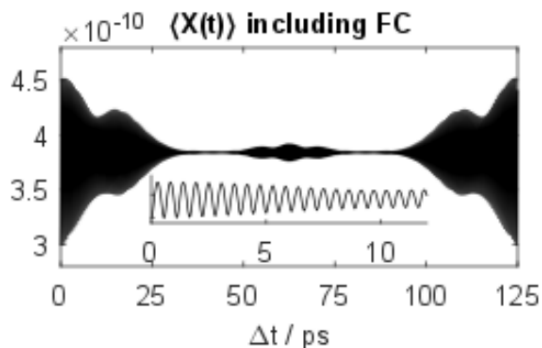
Figure 7: Expectation value of the position operator for the excitation of a diatomic molecule as a function of time. The spacial overlap of the initial and final state is considered. In the inset the oscillation of the position operator is shown. [14]

1.5 Femtosecond Pump-Probe Experiments

To study atomic motions that take place on very fast time scales, like the wave packet dynamic of molecular vibration, suitable experimental methods are needed. The typical experimental approach is a pump-probe scheme: A short, spectrally broad pump pulse creates a WP in an electronically excited state. A schematic representation of the typical sequence of a pump-probe experiment can be seen in figure 8 a. After its creation, the localised WP oscillates back and forth within the PEC. If the molecule does not dissociate, which is represented by the state C in figure 8 a, a probe pulse can ionize the molecule and the measurable photoelectron and -ion energies can be used to study the molecule under observation. If the transition moment to the ionized state is changing with internuclear distance, for example when the wave packet is moving in and out of a Condon point, the wave packet oscillation is reflected in the oscillation of the resulting photoelectron signal. Figure 8 b shows a schematic representation of these oscillations. The anharmonicity of the PEC leads to different energetic spacings between the vibrational states and leads thereby to different phase velocities for different vibrational states. Since the measured signal is a superposition of different vibrational states, the varying energetic spacings cause the WP to disperse shortly after its creation. If there is no interaction with the surrounding, the wave packet forms a revival with the same amplitude as the original oscillation (dispersion).

The theoretical dispersion time, that is the time until the wave packet has completely lost its initial localization, according to reference [15], can be calculated with the formular

$$\tau_{\text{disp}} = \frac{v * h^2}{(2 * \delta E * \omega_{\text{e}} x_{\text{e}})} \tag{12}$$

Here v equals the oscillation frequency around the wave packet energetic center, δE the energy differences between the lower and upper full width half maximum (FWHM) of the excitation pulse that generates the wave packet in the morse potential and $\omega_e x_e$ the anharmonicity of the excited state. This equation has been first calculated in reference [16] and recalculated in reference [15]. The calculated values for aluminium and indium are given in section 3.1.4.
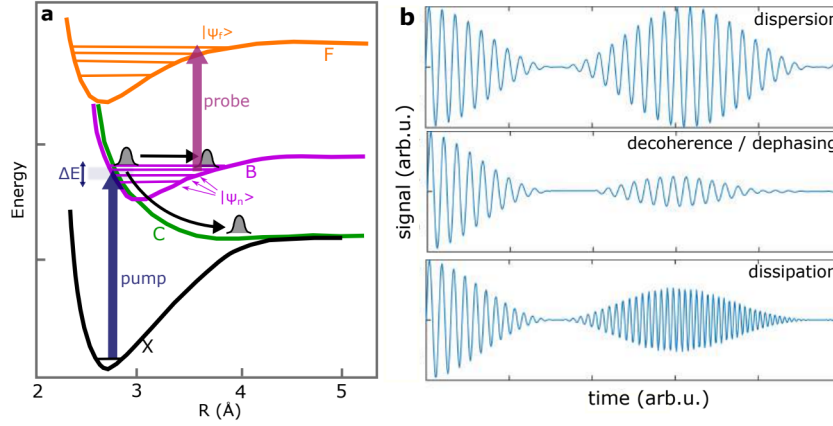

Figure 8: a.) Schematic representation of the typical sequence of a pump-probe experiment. A pump pulse excites several higher lying states which form a wave packet that performs an oscillating movement before the unharmonicity of the PECs lead to dispersion. If the wave packet does not transfer in another state C that represents the dissociation of the molecule, it can be ionised with a probe pulse. The photoelectron and -ion yield can be used to study the electronic structure of the dimer under investigation. b.) There are three transient signal changes that can be observed within the evolution of a wave packet: Dispersion due to anharmonicity of PECs, decoherence from elastic interactions with the environment and dissipation due to inelastic interactions. ([15])

If the interaction of the molecule with its surrounding is purely elastic, implying a loss in phase relation while the population of the vibrational levels is unchanged, there will just be an oscillation contrast decay (decoherence). If the molecule is subject to some external perturbation though, the collision of the molecule with other species will derogate the phase relation and also lead to vibrational relaxation (dissipation) to lower lying states. An increase of the vibrational frequency is a sign for coherent dissipation since the spacing of the PEC is getting narrower at lower energetic states.

Figure 9 shows the measured signals of a pump-probe experiment with I_2. The different vibrational states contained in the wave packet are revealed with its Fourier transformation in figure b, what displays the varying energetic spacings of the contained vibrational states [17]. In chapter 1.2.1 the Morse potential, which is an interatomic interaction model for the potential energy of a diatomic molecule, was explained. For a Morse potential the revival time can be calculated with the following formula [18]:
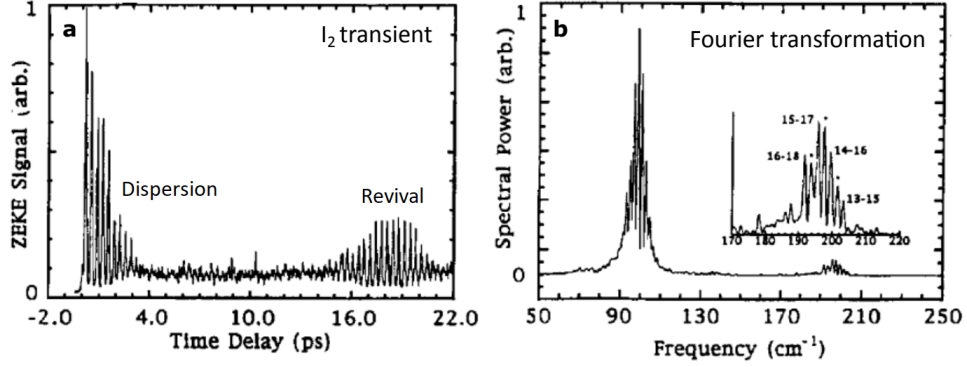
Figure 9: Measured signals of a pump-probe experiment with I_2 a.) The Time-resolved Zero Electron Kinetic Energy signal exhibits the wave packet oscillation directly after the creation of the wave packet and within the revival that forms after about 17 ps. The amplitude of the revival is lower due to relaxation in lower lying states, equivalent to the state C schematically represented in figure 8. b.) The transient signal's Fourier transformation shows the vibrational beat frequencies of the anharmonic PEC of I_2 for the nearest-neighbour levels at about 100 cm^{-1} and next nearest neighbour levels at around 200 cm^{-1}. (Figure taken from [17])

$$T_{\text{rev}} = \frac{1}{\omega_e x_e} \tag{13}$$

$\omega_e x_e$ represents the anharmonicity of a Morse potential. If no interaction with the environment takes place, all vibrational states are in phase again at the revival time and the WP shows the same localiced features as immediately after its creation. At the so called half revival time $T_{\text{rev}/2}$ also all wave functions are in phase. Although the phase of all wave functions is shifted 180 °, the electron- and ion yield should be the same as at the full revival. The process of dispersion and the formation of a revival is shown in figure 9 a.

To observe molecular dynamics that are happening on the fs and ps time scale, like vibrational wave packet oscillations, a suitable setup for conducting pump probe experiments is needed and the measurement data have to be analysed in a temporal and frequential domain.

2 Experimental Setup and Data Analysis

In this chapter the experimental setup and subsequently the method for data analysis of the PE spectra will be explained. Also the experiences with different crucible setups for the aluminium pickup and the setup parameters of successful measurements will be discussed.

2.1 Helium Nanodroplet Environment

To be able to observe molecular dynamics, like wave packet oscillations, and avoid decoherence and dissipation as far as possible, an environment that does not interfere with the system is favourable. For many molecular systems, photo excitation would also not be possible because of their instability or destruction due to the pulse energy. To achieve active stabilization, the photo pulse energy can be dissipated into a thermal bath, a strategy that was already pursued by Zewail et al. [19] and is exploited in matrix isolation [1]. Due to their superfluity and weak interaction with dopants, helium nanodroplets (HeN) are favoured to be used within spectroscopic experiments in femtochemistry, that studies dynamical processes. They offer the possibility to capture dopants, stabilize their bonds and just weakly influence them.

In solvents, decoherence times of molecular dynamics are typically in the fs range, and can only in special cases, as well as in cryogenic rare-gas matrices, range up to a few ps [20] [21]. For the case of alkali metal dimers on the surface of He_N a range from weak (~ 1.5 ns) [22] to strong decoherence (~ 5 ps) [23] has been found.

For In_2 in the He_N's interior, where the influence on the dopant is much stronger, we have found that coherence can last 50 ps and longer, exceeding decoherence times of conventional solvents by a factor of 10–100 [24]. He_N have the property of cooling most energetic degrees of freedom to investigate weakly bound systems. This combination of low temperature (0.4K), high spectral transparency ($<24eV$) and inertness of the helium host allows the controlled synthesis and investigation of also species that are fragile, reactive or tailor-made aggregates [25]. Further benefical properties of He_N include the ability to easily use sequential pickup techniques, enabling the formation and stabilization of multi-species systems, like microsolvation environments [8]. Within the experimental setup they are loaded with foreign atoms or molecules by letting them pass through a pickup cell that contains the desired species at a sufficient vapour pressure [15]. This is a requirement for microsolvation. A detailed description of the experimental setup is given in the following.

2.2   Experimental Setup

The investigation method used in the course of this thesis was a pump probe scheme with femtosecond time resolution, which has been addressed in chapter 1.5 already, in the course of explaining the pump-probe scheme. The system under investigation were Al_2 doped superfluid He nanodroplets. The experimental setup is schematically shown in figure 10. The laser pulses are generated with a commercially available titanium-sapphire laser system (Coherent Vitara oscillator, Legend Elite Duo amplifier). The obtained pulses have a duration of 25 fs with a repetition rate of 3 kHz. The average power is 13 W and the center wavelength is 800 nm. To conduct a pump-probe experiment, a beam splitter (BS) is used to generate a pump and a probe beam. The pump beam can be frequency upconverted in an optical parametric amplifier (OPA, Coherent OPerA Solo) to any desired wavelength between 240 and 2260 nm. The probe beam is guided across a translational delay stage, to provide a variable time delay between the pump and the probe pulse. When optimally adjusted, the full stage length of 10 cm can provide a maximal delay of 300 ps. A set of four optical elements provides third harmonic generation (THG) for the output of about 270 nm. A beta barium borate (BBO) crystal is used for second harmonic generation (SHG) to frequency upconvert the pulse to about 406 nm. A time delay compensator (TDC) crystal is used to compensate the group velocity dispersion that is about to happen within the sum frequency generating (SFG) crystal. A lambda-half-plate is used to get approximately a 1:1 ratio of the fundamental and the second-harmonic photons. After the SFG crystal, the THG and the OPA beams are aligned again using a T-mirror and focused into the chapter with a lens with a focal length of one meter.
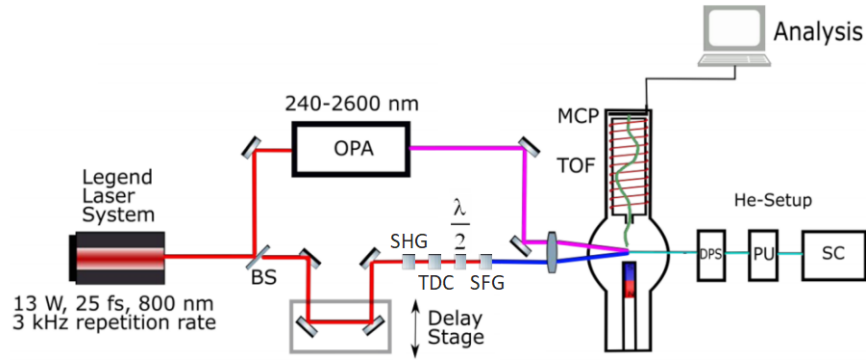
Figure 10: Schematic drawing of the experimental setup - A Laser system produces a 800 nm beam that is split into two beams. One of those is directed into an OPA, that is able to produce wavelengths between 240 and 2600 nm. The second beam has a path that uses a delay stage to vary the time delay between the two pulses. For this pulse we use third harmonic generation to produce a wavelength of about 270 nm.
BS... beam splitter, OPA... optical parametric amplifier, SHG... second harmonic generator, TDC... time delay compensator, SFG... sum frequency generator, TOF... time of flight mass spectrometer, MCP... Microchannel plate detector, DPS... differential pumping stage, PU... pickup chamber, SC... source chamber (altered figure from reference [14])

A brief explanation of the properties and advantages of He$_N$ was given in chapter 2.1. For this pump-probe experiments also a beam of superfluid He nanodroplets is generated in a supersonic expansion. High purity He at 20 bar stagnation pressure is thereby expanded from the source camber (SC) through a precooled nozzle of 5 μm diameter. The nozzle is operated at the lowest possible temperature of 11-11.75 K and thereby generates He$_N$ with the highest possible particle number, what turned out to offers the best condition for a high pickup of aluminium and aluminium dimers (Al$_2$) in the pickup (PU) chamber. After the PU, the He$_N$ beam passes through a differential pumping stage (DPS) and then intersects with the laser beams in the main chamber. To find the spacial overlap of the two laser beams, the beams can be redirected at the optical table onto a CCD-camera that is used for the rough adjustment. To find the temporal overlap, it has to be ensured that the overlap is within the range of motion of the delay stage and subsequently the stage can be scanned and a peak (non-resonant excitation) or a step (resonant excitation) in the electron yield indicates a superimposition of the two separated beams again. The pump pulse excites the dopant within the He droplet and the time delayed probe pulse ionises it. With a magnetic bottle type time of flight (TOF) spectrometer and a microchannel plate (MCP) the photoelectrons and photoions can be measured. A repeller beneath the beams uses high voltages to accelerates ions towards the detector. The electrons are guided to the detector with the magnetic field. The repeller voltage can be adjusted to increase resolution.

2.3 Pickup of Al$_2$

The construction of a setup for the evaporation of aluminum turned out to be a difficult task. Its high reactivity and evaporation temperature gave rise to the challenge of finding a new setup suitable for the examination of this substance. First, the old setup with Al$_2$O$_3$ ovens, that have been used for the experiments with indium and magnesium, will be discussed. Subsequently the operating conditions for the new BN-crucible setup, particularly acquired for experiments with aluminium, will be looked at.

2.3.1 Pickup with Al$_2$O$_3$ Crucibles

Since aluminium has a lower vapour pressure than indium and magnesium, there was the need to heat up the pickup oven to higher temperatures. Figure 11 shows the vapour pressure of the three specimens for the respective pickup-oven heating currents.
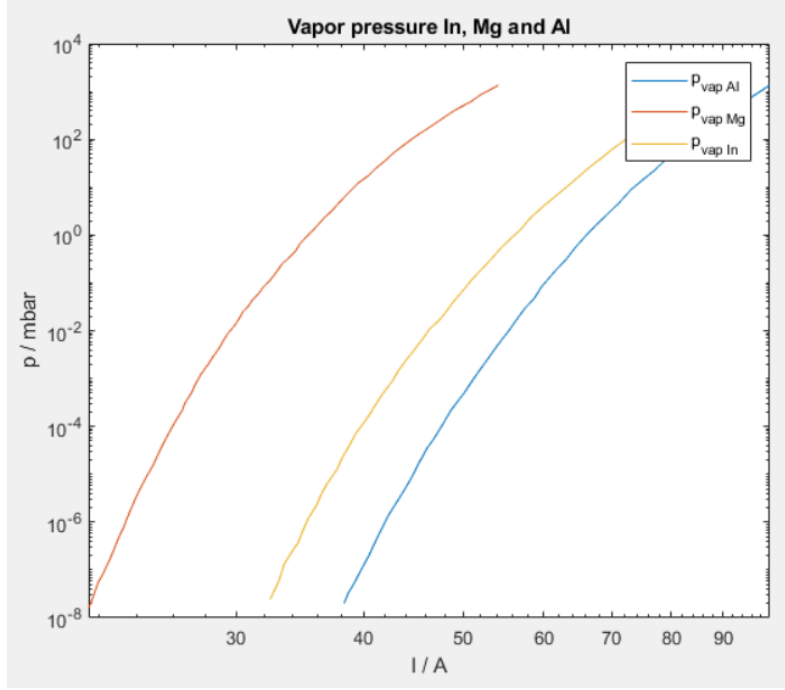
Figure 11: Al_2O_3 crucibles temperature needed to obtain a vapour pressure for sufficient dopant pickup with different molecules - The current dependend crucible temperature has been obtained from another research group in the department and the vapour pressure for each temperature has been retrieved from [26].

Indium has been investigated at a pickup current of 43 A, and thus a pickup pressure of $1*10^{-3}$ mbar, and for magnesium a pickup current between 26 A and 28.8 A, what yields a pickup pressure of about $2*10^{-3}$ to $5*10^{-5}$ mbar, was used. To obtain a similar vapour pressure as magnesium, a pickup current between 46.3 and 52 A was needed for the heating of aluminium with the Al_2O_3 crucibles. The best pickup conditions for aluminium where obtained with the lowest nozzle temperature achievable. This might be because smaller droplets possibly did not overcome the passing of the high temperature oven.

Figure 12 shows the QMS-signals from four different masses relevant for the experiment. With rising temperature, the amount of helium detected was continuously falling, whereas the aluminium signals where rising first, because the vapour pressure and thereby the pickup was rising. It is well observable that the monomer signal has its maximum at 50 A, whereas Al_2 has its maximum at 51.5 and 52 A. At these currents the helium signal had decreased to 56 percent.
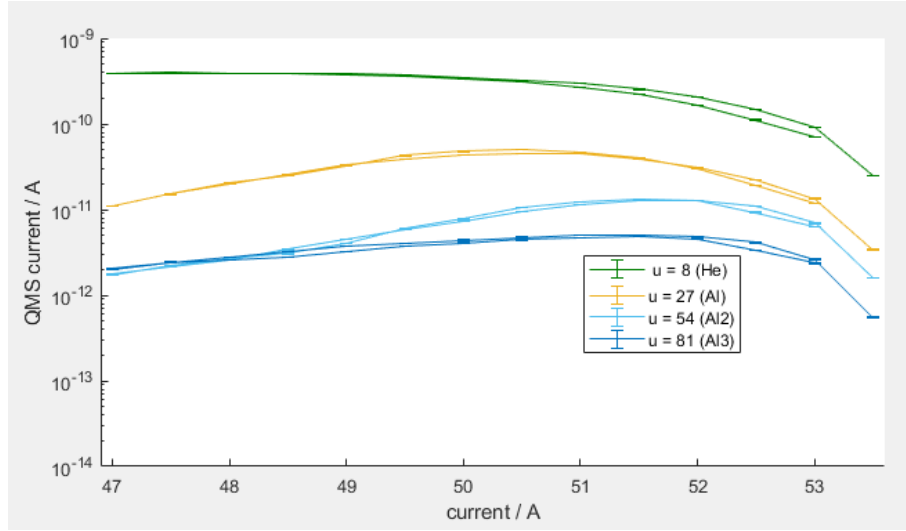
Figure 12: Pickup scan with QMS for the masses of He, Al, Al_2 and Al3. The Al_2 dimer has the highest pickup at 51.5 and 52 A.

Aluminium is more sensitive to heating than former investigated elements. Firstly, besides having a high melting temperature, it also has a relative high specific heat capacity of 0.90 J/gK, compared to other metals like indium with 0.23 J/gK. Secondly, it forms a wetting layer. This combination puts a lot of stress on the oven pots and makes slow heating recommendable. Beneath 30 A, it was advisable not to exceed a current change of three ampere per hour when using Al_2O_3 pots, to avoid fracture. Above 30 A, the temperature changes and thereby the stress on the oven pots are not that high anymore and heating can be done in the order of 12 ampere per hour.

2.3.2   Pickup of Aluminium - Problems, Approaches and Findings

A previously unknown problem arose from the high reactivity of aluminium. Aluminium seemed to performed a reaction with the previously used Al_2O_3-crucibles by reducing pots and rupturing it. Figure 13 a shows a ruptured pair of crucibles.
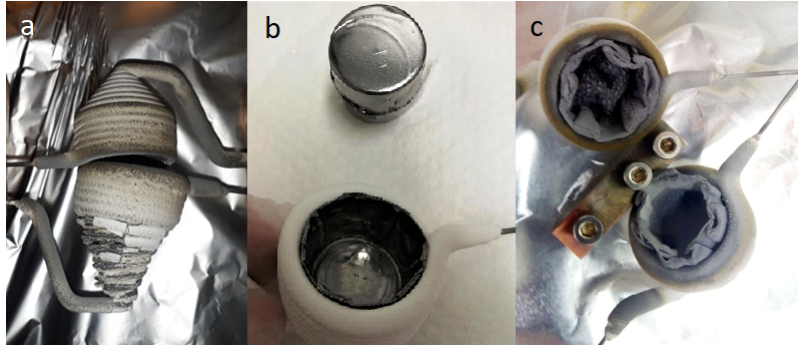
Figure 13: Al$_2$O$_3$-crucibles - a.) A ruptured pair of crucibles not suitable for the investigation of Al$_2$. b.) Al$_2$O$_3$-crucibles with tantalum cups to reduce infiltration and increase the vapour pressure c.) Aluminium alloy of tantalum cups inside the Al$_2$O$_3$ ovens

The heating for a sufficient pickup up to 51 A was demanding on the material. To increase the vapour pressure and also hinder the aluminium to infiltrate the Al$_2$O$_3$-crucibles, tantalum cups were installed, like visible in figure 13 b. Tantalum also alloys with aluminium and was able to infiltrate the Al$_2$O$_3$-crucibles, as visible in figure 13 c.

Since this setup was not usable for the work with aluminium anymore, a new solution was needed.

2.3.3 Tungsten Basket Heaters with Boron Nitride Crucibles

The switching to Boron Nirtide (BN) crucibles with tungsten wire mounting, like recommended by the manufacturer for the investigation of aluminium, was an attempt to minimize the emanating aluminium. Small openings were drilled into two otherwise completely closed baskets to increase the vapour pressure inside the crucibles. Thereby the needed temperature and overall evaporating aluminium should be lowered to protect the material from fraction. Although aluminium and nitrogen also react to AlN, the ceramic structure of BN is more stable. Concerning the basket heaters, Al reacts with tungsten, tantalum and molybdenum [27]. No good alternative to tungsten was found yet. Although it alloys, the high melting point of tungsten is needed to reach the required vapour pressure to generate Al$_2$. [28]

Due to less resistance of the tungsten wires compared to the former used Al$_2$O$_3$-crucibles, higher power from the current source was needed. In the course of the crucible exchange also the current source was changed. To reach a vapour pressure that is high enough, we build a tantalum shield to increase the temperature inside the pots. Previously, the tantalum pots were used to increase the vapour pressure by reducing the effusing aluminium. The tantalum shield uses reflection to increase the temperature and thereby the vapour pressure.

In figure 14 one can see that aluminium forms alloys with tungsten and also tantalum and infiltrated the tungsten wires and the tantalum shield that was build of several tungsten layers. The infiltration of the tungsten layers made them swell and lead to electric contact between the shield and the tungsten wires. Also the ruptured tungsten wires broke apart and formed a new connection, as visible in figure 14.
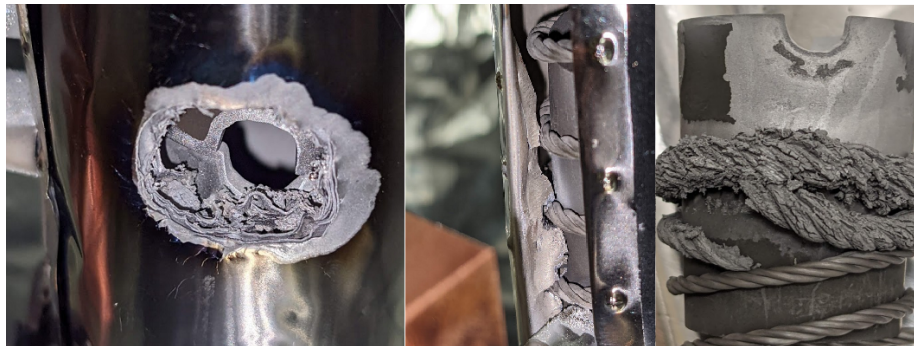

Figure 14: Alloyed tungsten shield and ruptured tungsten wire basket (Lab.book: 26.05.2021)

If a tantalum shielding has to be used again, less layers and more distance to the wires is recommended.

New crucibles and wires should be usable for a measuring period of several weeks. Since aluminium reacts also with tungsten, it will eventually infiltrate the wires and rapture them. Aluminium also covers these crucibles, that is why the whole setup always has to be exchanged at once. Although aluminium alloys tungsten, the high heat resistance is needed and so far there is no alternative to this setup.

2.4 Experimental Approach to Find Molecular Dynamics

In the following the approach for the search for molecular dynamics will be presented. As first step in finding a molecular state, the excitation photon energy has been varied from 290 nm to 355 nm in 5 nm steps and the photoelectron counts were investigated.
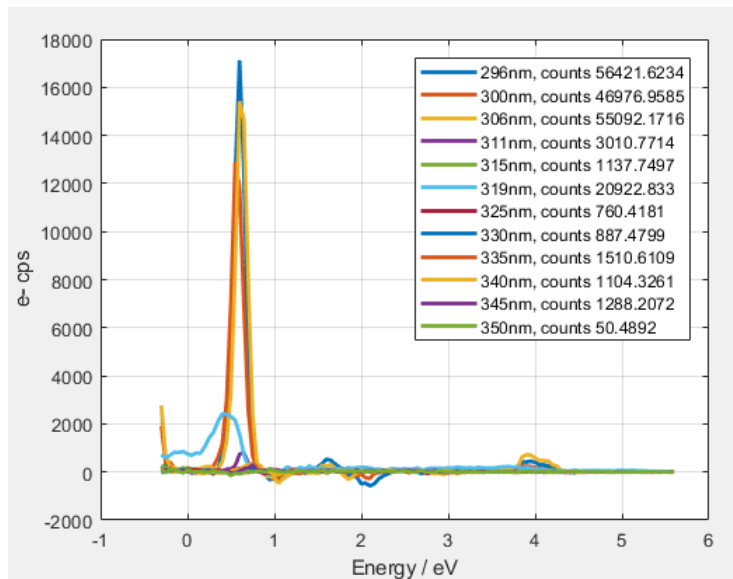
Figure 15: Photoelectron spectra of the investigated wavelengths

In figure 15 the photoelectron (PE) spectra for pump only excitations are shown. Four excitation wavelengths, namely 293, 304, 318 and 330 nm, have been chosen to further examine by varying the pickup temperature.

The states could be assigned to monomeres or dimers according to their broadness and temperature dependent behaviour. Dimere states need higher temperatures because not only one but two Al atoms are needed and they have an energetically broader spectrum compared to monomere states.

At the previously most promising wavelength 297 nm there was no pump probe excitation of dimers identifiable, what has been ascribed to the strong resonance at the pump only wavelength and the depopulation of states. Reference [12] also states, that the E'-state, that is likely to be excited at this wavelength, is also decaying fast and might not have been observable if there was not a good temporal overlap.

The electron spectra however show a potential pump probe dimer excitation around 319 nm. At this excitation wavelength there was a stable state found, most likely the E-state, that also shows molecular dynamics.

2.4.1 Parameters for the Observation of Molecular Dynamics of Al$_2$

Besides the right excitation wavelength a lot of other parameters have to be set right to construct the right conditions for coherent molecular dynamics and their observation. Table 1 gives a comprehensive overview of the parameters that were set and made the observation of vibrational dynamics of Al$_2$ possible with each of the crucible and current source setups.

Table 1: Parameters for the two different oven and current source settings that made the observation of molecular dynamics possible

Parameter	Unit	Al$_2$O$_3$ crucibles (Lab.book 01.12.2020)	BN crucibles (Lab.book 21.05.2021)
p$_{He}$	bar	20	30
T$_{nozzle}$	K	11.3	12.3
I$_{PU}$	A	51	92
P$_{PU}$	W	357	810
Further settings	-	Second PUC-oven	With Ta-shield
N-trap	-	Not used	Not used
U$_{Repeller}$	V	-0.3	+1.4
wl$_{pump}$	nm	319.5	319.4
P$_{pump}$	mW	35	35
wl$_{probe}$	nm	269.6	264.2
P$_{probe}$	mW	2	3-5

An important parameter is the right repeller voltage for the observation of the dynamics. A too high positive voltage might hinder photo electrons to reach the MCP and a high negative voltage reduces the contrast. Interestingly, within the first measurements a negative repeller voltage of -0.3 V was used while in the second successful measurements a positive voltage of 1.4 V had to be applied to obtain a signal.
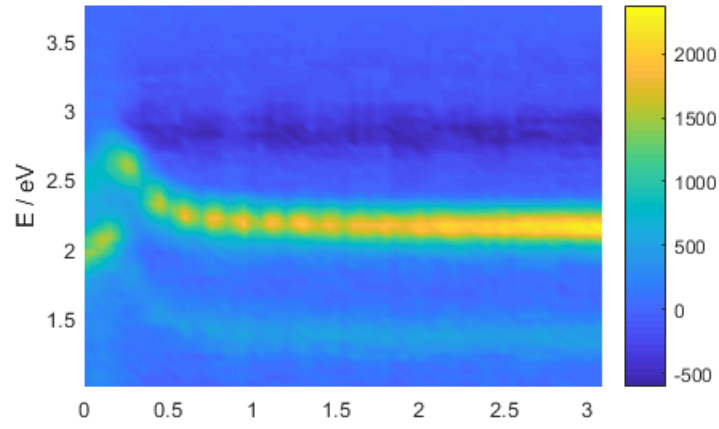
Figure 16: Energy calibrated PE time scan of first measurement period (Lab.book 03.12.2020)
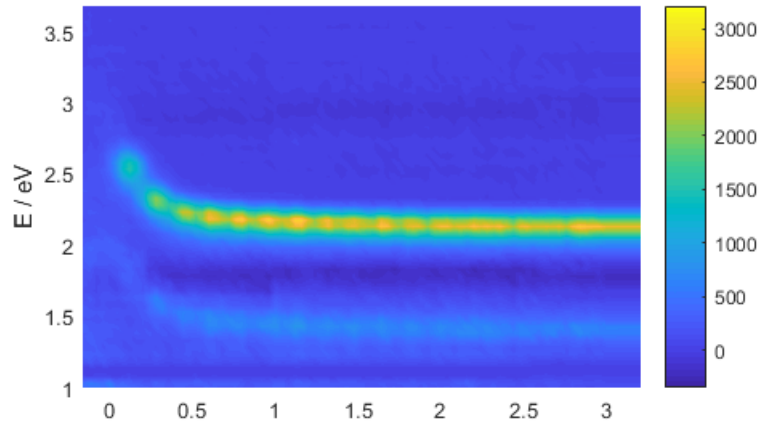
Figure 17: PE timescan of second measurement period. PE time scan has been calibrated afterward to fit to calibrated measurements of first measurements from december 2020. (Scan 203, Lab.book 20.05.2021)

Figures 16 and 17 show the original oscillations of coherent molecular dynamics in Al$_2$ with two different setups. In both measurements two states are visible. Both spectra show a lower energetic, weaker band and a higher energetic stronger band.
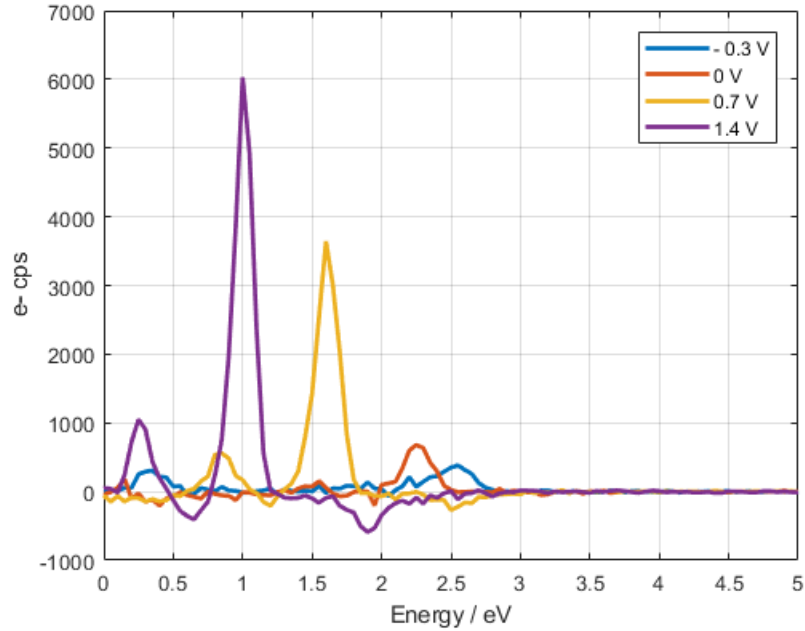
Figure 18: PE spectra at different repeller voltages - The first measurements have been conducted with -0.3 V. With the second setup 1.3 V were needed to observe the molecular dynamics. The calibration was done at -0.3 V.

In an attempt to restore the first measurement, also within the second series the repeller voltage of -0.3 V was used first. In figure 18 four different voltages and their associated PE spectra are shown. At -0.3 V, which was the repeller voltage used at the first measurement period, there was no state visible. With increasing voltage the dynamic became visible. The variation in the needed repeller voltage might stem from the change of the evaporation setup between the measurements, which might have influenced the pickup conditions of the He_N droplets.

Furthermore the probe-pump state of the first measurement period is missing in the second measurements which can be ascribed to a different heating temperature. If the temperature with the Al_2O_3-crucibles was higher, this state could be ascribed to Al_3. Also, the bleach that was first at higher energies, is energetically below the dynamic within the second measurements.

2.5   Sliding Window Fourier Transformation

The PE spectra, which can be seen as fingerprints of the wavepacket oscillation, were analysed using sliding window Fourier transformation (SWFT). A detailed description of which can be found in reference [14] and the following should give a short overview. The general idea is to analyse a timescan to determine for which times which frequencies and corresponding amplitudes are contributing to the signal. Therefore, intervals of the timescan are analysed with Fourier transformations and the frequency components of this sliding windows are recorded for each time window. This results in a time and frequency-resolved Fourier spectogram. The size of the intervals should depend on the frequency to be resolved. Figure 19 shows the transient PE spectrum and its integrated signal for the first revival. One can see the window size of 2.4 ps that has been chosen for the analysis of some of the scans in this thesis.
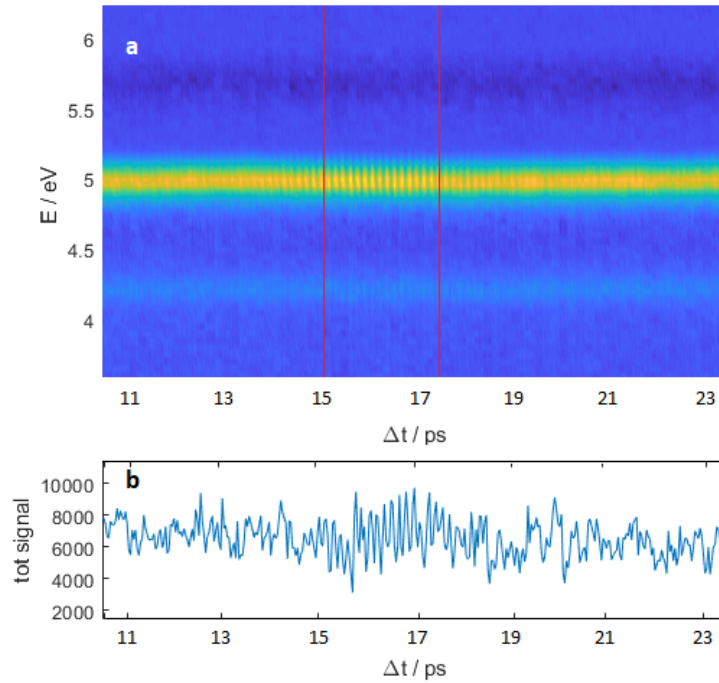
Figure 19: First revival: a.) Transient PE spectrum b.) Integrated transient PE spectrum - (Lab.book: 01.12.2020, startfile: 55476)

Figure 20 displays the Fourier transformation of the whole scan of which figure 19 shows a part of the scan. The first 2 ps have been excluded from the SWFT. The frequencies beneath a certain threshold, in this case 4 THz, can be regarded as background. For the further analysis these frequencies have to be cut out to get a signal that oscillates around zero.
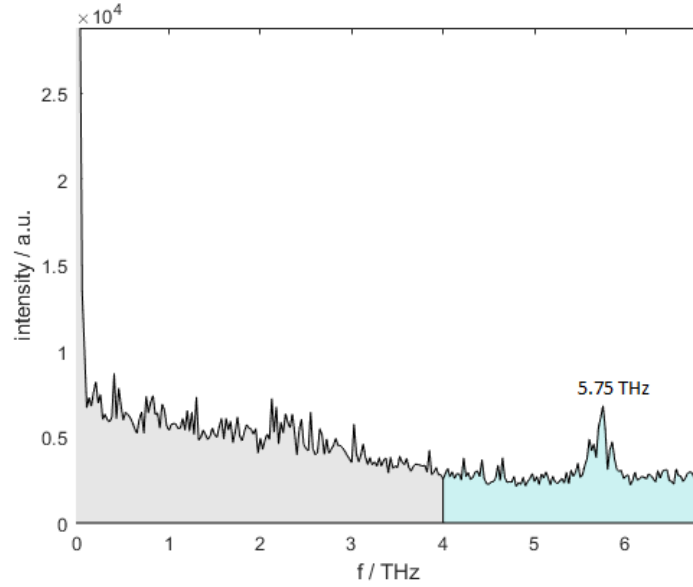
Figure 20: Fourier transformation of the full transient PE spectrum - The first 2 ps have been excluded from the SWFT. Frequencies beneath a certain treshold, in this case 4 THz, can be regarded as background. (Lab.book: 01.12.2020, startfile: 55476)

For the analysis of the temporal evolution of the molecular dynamic of aluminium, a window size of 60 points was chosen. Depending on the stepsize, for which 0.04 ps and 0.05 ps were chosen, that corresponds to a time window of 2.4 ps or 3 ps. For the determination of the frequencies at each revival, the whole measurement window of 6 ps was taken for the timescans 203-208, which corresponded to a window size of 100 points. The window function used for the analysis is a Hamming window function, as displayed in figure 21.
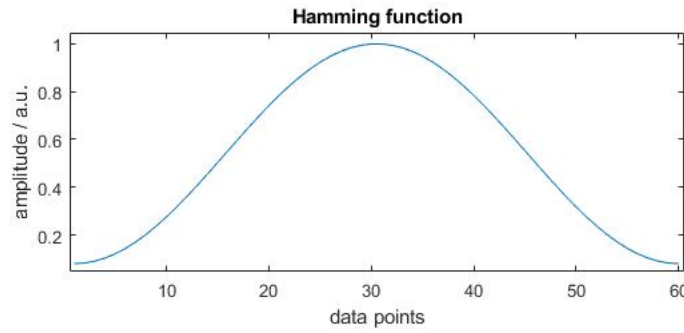
Figure 21: Hamming window for 100 points like used in the Sliding Window Fourier transformation of a transient PE spectrum

Within the SWFT the signal within the time window is pointwise multiplied with the window function and integrated for that time window. Figure 22 shows the energy resolved SWFT of

the above introduced PE spectrum.
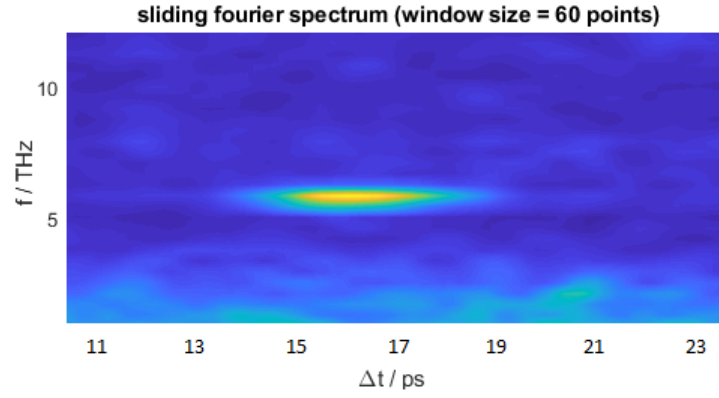
Figure 22: Sliding Window Fourier transformation of a transient PE spectrum (Lab.book: 01.12.2020, startfile: 55476)

A detailed description and the Matlab code for the SWFT can be found in reference [14].

3   Results

Within this thesis, molecular states of Al_2 were investigated that can be excited within 315.1 and 319.9 nm. In the beginning the general outcome of the work from this thesis will be given. Subsequently additional experimental results will be shown.

Table 2 summarizes the measurements that have delivered interesting results. The numbers of the most useful ones are displayed as bold. In the first measurement period in November and December 2020, the same Al_2O_3 crucible setup, that has also been used with indium and magnesium, was used. Due to the high reactivity of Al_2 it was switched to BN-crucibles for the second measurement period in May 2021. In the next section the most important findings will be discussed. The scan with start number 55476 is the only full PE scan up to 50 ps. Mainly this scan will be used to give an overview of the parameters that can be measured within this experiments. With timescan 194 the revival times where determined and the evaluation at further time delays is done for the scans 203, 205, 207 and 208 that show revivals of the molecular dynamics up to 200 ps.

Table 2: Settings of useful measurements
Nr ... (start-) number of timescan, λ_{pu}... excitation wavelength,
λ_{pr}... ionisation wavelength, tv ... time vector, tw ... time window,
p_{He} ... Helium pressure, T_{noz} ... Temperature nozzle, P_{PU}... Pickup chamber pressure,
U_{Rep}... Repeller voltage, P_{pu}... Power pump pulse, P_{pr}... Power probe pulse

Date	30.11.2020	01.12.2020	03.12.2020	20.05.2021	20.05.2021
Nr	54092	**55476**	**58984**	192	**194**
λ_{pump}/nm	317.8	319.5	315.1	319.9	316.8
λ_{probe}/nm	402.4	269.6	269.6	264.2	264.2
tv	0:0.03:12	0:0.04:50	0:0.05:131	0:0.05:2, 13:0.05:15	0:0.05:25, 120:0.05: 132
tw	-	-	6 ps	-	6 ps
p_{He}/bar	20	20	20	30	30
T_{noz}/K	11.3	11.3	11.3	11.24	12.24
P_{PU}/W	357	357	357	789.6	809
U_{Rep}/V	0.3	-0.3	-0.3	1.4	1.4
$P_{\mathrm{pu}}4$/mW	-	36	25	40	35
P_{pr}/mW	-	3	7	4	4
notes	with SHG				find t_{rev}
Figure / Page	59 / 66	25 / 35	49 / 58		29 / 39

Date	20.05.2021	21.05.2021	21.05.2021	21.05.2021	21.05.2021
Nr	200	**203**	**205**	**207**	**208**
λ_{pump}	316.8	319.4	319.4	319.4	319.3
λ_{probe}	264.2	264.2	264.2	264.2	264.2
tv	0:0.05:50	0:0.05:220	0:0.05:210	0:0.05:140	0:0.05:210
tw	3 ps	6 ps	6 ps	6 ps	6 ps
p_{He}/bar	30	30	30	30	30
T_{noz}/K	12.3	12.3	12.3	12.3	12.3
P_{PU}/W	809	809	809	809	809
U_{Rep}/V	1.4	1.4	1.4	1.4	1.4
P_{pu}/mW	35	35	35	35	35
P_{pr}/mW	4	4	4	4	4
notes	wrong interval		high resolution windows		
Figure / Page		40 / 50	51 / 60	53 / 62	57 / 64

3.1   Main Measurement Results

The measurement results fit well to one of the aluminium dimer states that were measured in jet-cooled gas phase. The following sections will show the most important findings.

3.1.1   Wave Packet Formation within the E-state

Figure 23 shows the vibronic lines of the $E2^3\Sigma_g^-$ state, which has been introduced in section 1.2.3 already and will subsequently be refered as the E-state, and an excitation pulse with a FWHM of 3.4 nm. The potential energy curves of the electric states of Al_2 can be seen in figure 24. The E-band spans from 369.0 nm to 323.6 nm in gas phase and the shift of 0.4 eV due to the bubble expansion of the helium, which will be explained in section 3.1.4, is shifting the E-state (36 ± 15) nm to lower wavelengths. The high uncertainty stems from the fact that the ionic state is shifted in the opposite direction than the excited state due to the helium and thereby increasing the bubble expansion. The bubble expansion will be addressed in section 3.1.5. Therefore the sole energy shift of the E-state is smaller than the measured bubble expansion. A pump pulse with 319 nm is exciting approximately the center of the E-state in this helium environment, as visible in figure 23. The splitting between the highest frequency vibrational state lines is (30.4 ± 0.4) cm^{-1} and between the lower state lines it is (33.0 ± 0.5) cm^{-1}. This consideration yields 15 contributing vibrational states in the generated wave-packet.
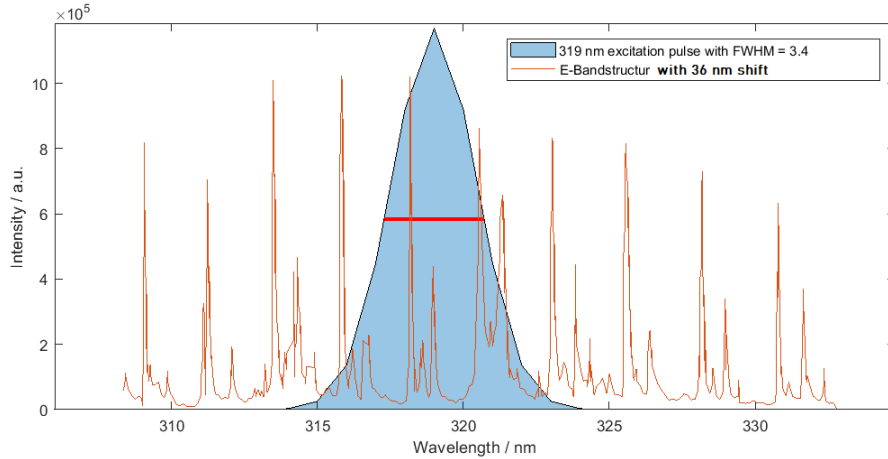
Figure 23: Vibronic excitation spectrum of the E-state with (36 ± 15) nm energy shift due to the helium environment and a 319 nm pump pulse. The vibronic excitation spectrum of the E-state in gas phase stems from reference [12]. The high uncertainty stems from the fact that the ionic state is shifted in the opposite direction than the excited state due to the helium and thereby increasing the bubble expansion. The bubble expansion will be addressed in section 3.1.4. Therefore the energy shift of the E-band is in fact smaller than the measured bubble expansion.
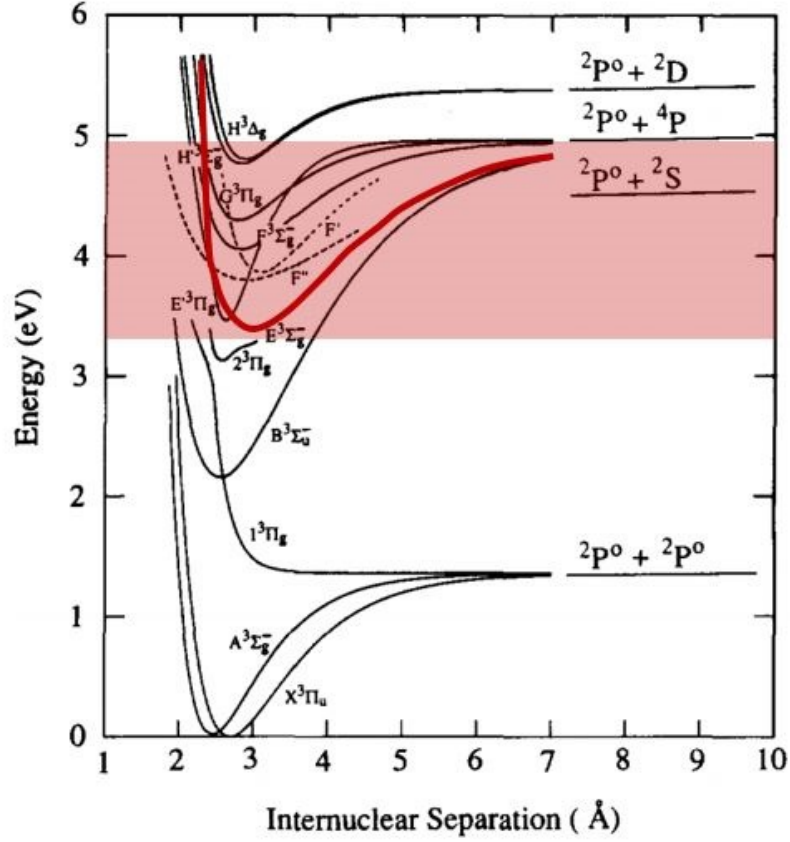
Figure 24: Schematic potential energy curves for the electronic states of Al$_2$ and two ground states. The red area marks a reagion in which molecular dynamics are continuously observable, stemming from different states. The red line marks the E-state that has an experimental oscillation period and revival time within our experiments that matches the results of former experiments in gas phase. Altered figure from reference [12]
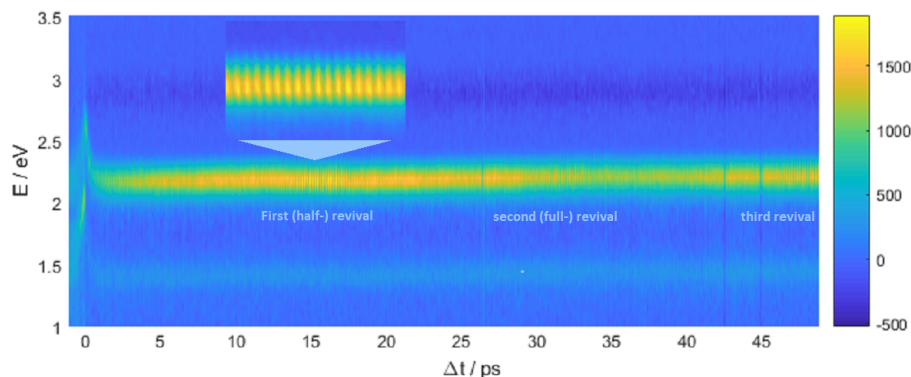
Figure 25: PE timescan of an excitation with 319.5 nm pump wavelength and 269.6 nm THG probe pulse. The original oscillation and three revivals are visible. (Lab.book: 01.12.2020)

Figure 25 shows a full timescan of the Photoelectron (PE) energy signal of the first 50 ps after photoexcitation. The PE energy is serving as a fingerprint of the molecular dynamic of the excited state. After the excitation with the pump pulse, several excited states are forming a coherent wavepacket that is oscillating within the potential energy curve. After several ps the oscillation is dispersing due to the varing oscillation periods of the contributing states, like stated in section 1.5 and figure 8. At the revival times the wavepacket is restored and the oscillation in the PE signal visible again. At the beginning one can observe the helium bubble expansion, which will be explained in section 3.1.4. One can see that there are two states present, one settling at 2.1 eV and a lower weaker signal settling at 1.45 eV. The original oscillation and three of the subsequent revivals are visible. The first revival is suspected to be the half revival of the E-state, making the second weaker revival the first full revival of the dynamic.

3.1.2   The Wavepacket Oscillation Period

The PE timescan can be analyzed with SWFT, which has been explained in chapter 2.5, to retrieve the oscillation frequency of the generated wavepacket. The SWFT of the signal from figure 25 is visible in figure 26. A windowsize of 60 points has been used what includes 14 oscillation periods.
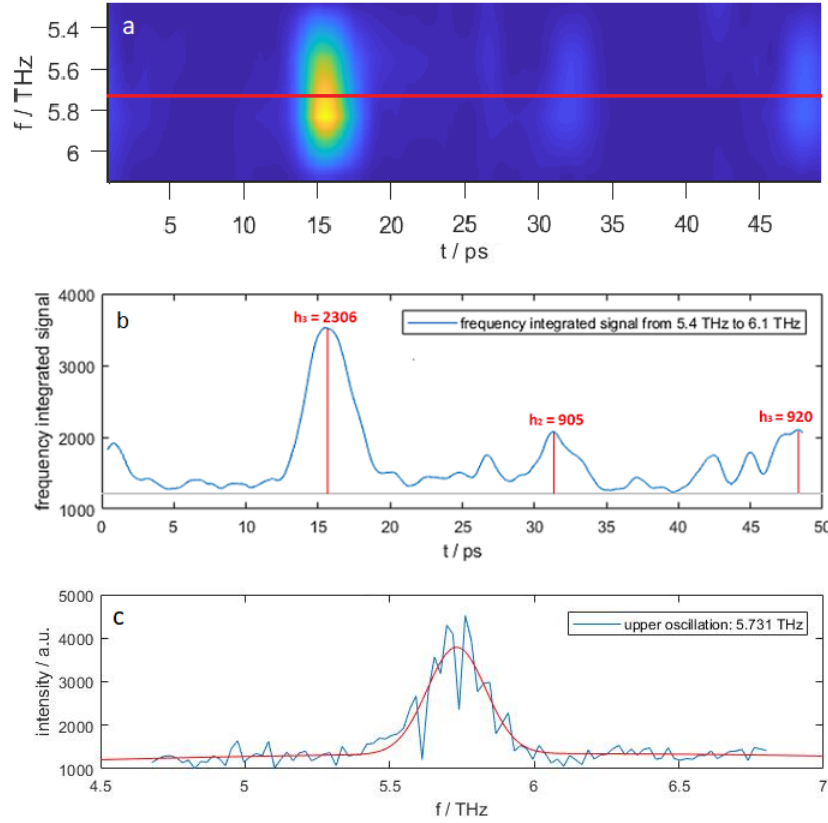
Figure 26: Sliding window Fourier transformation of the upper oscillation of figure 25 with 319.5 nm pump wavelength and a windowsize of 60 points, including 14 oscillation periods. a.) The SWFT shows that the oscillation frequency stays constant for the first three intervals. The signals at 26, 43 and 45 ps are artifacts stemming from a pressure drop in the cooling water system. b.) The frequency integrated scan shows the rise in signal at the revival times. The first revival shows a revival duration of (4 ± 0.2) ps and the second revival a revival duration of (3.2 ± 0.4) ps. c.) The wavepacket frequency of the upper oscillation lies at (5.73 ± 0.13) THz. (Lab.book: 01.12.2020)

Here just the upper, stronger oscillation is analysed. Figure 26 a shows the frequency resolved SWFT and in figure b the frequency integrated signal from 5.4 THz to 6.1 THz is visible. One can observe that, within this integration frequencies and after subtracting the background, the first revival has an integrated signal maximal of 2306 while the second and third revival have an integrated signal maximal of 905 and 920. That gives a ratio of 2.5 to 1 for the first oscillation to the second and third one. Figure c shows that the stronger upper oscillation has a frequency of (5.73 ± 0.13) THz.

(a) First revival of upper oscillation

(b) First revival of lower oscillation

(c) SWFT of whole measurement
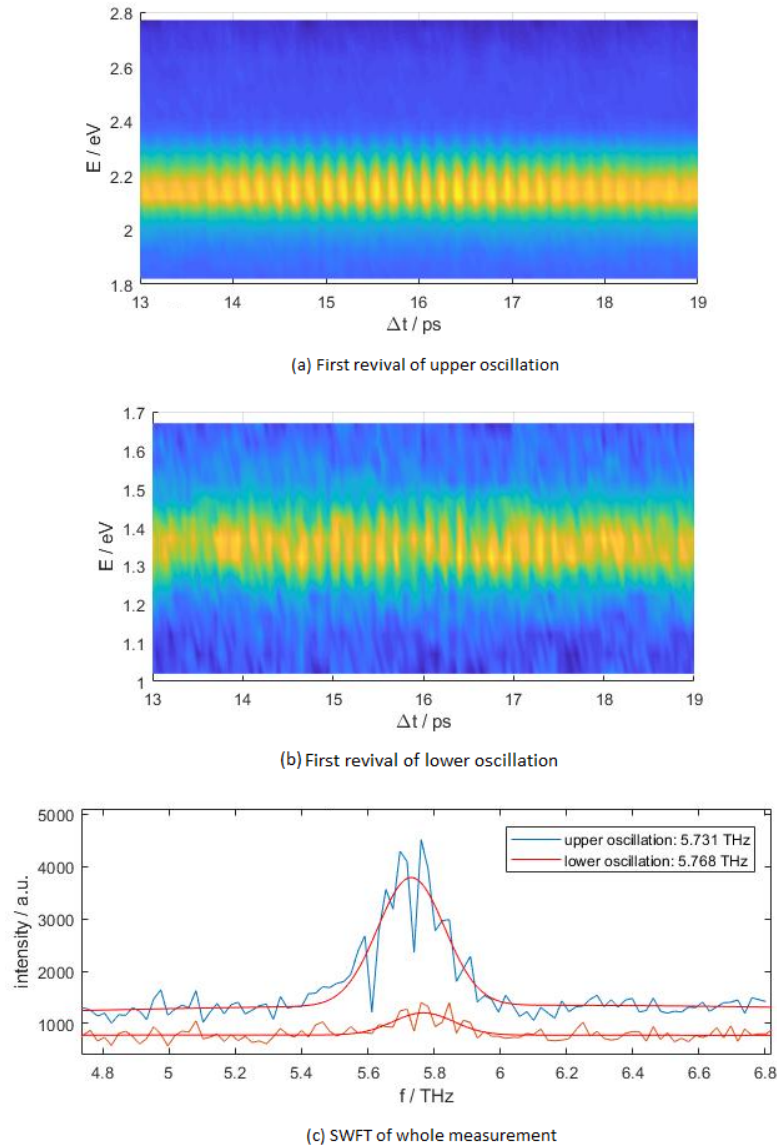
Figure 27: The upper and the lower oscillations with 319.5 nm pump wavelength and 269.6 nm probe wavelength. (a) PE spectrum of the first revival of the upper oscillation (b) PE spectrum of the first revival of the lower oscillation (c) SWFT of the whole measurement with a window size of 60 points, corresponding to 2.4 ps and 14 oscillation periods of the E-state dynamic - upper oscillation: (5.73 ± 0.13) THz and lower oscillation: (5.77 ± 0.08) THz (Lab.book: 01.12.2020)

In figure 27 both state signals, the upper and lower one at the first revival, are analysed. The SWFT of the measurement gives the following results:

$$\text{upper oscillation:} (5.73 \pm 0.13) \text{ THz}$$

$$\text{lower oscillation: } (5.77 \pm 0.08) \text{ THz}$$

The lower oscillation is thereby not significantly higher in frequency than the upper one.

3.1.3   Revival Period and Dispersion Time

The retrieving of the revival period is shown in figure 28 and figure 29. Figure 28 shows the PE timescan of the first 25 ps and the scan over the eighth revival with 319.9 nm pump and 264.2 nm probe wavelength and the SWFT of the PE timescan.

(a) Transient PE timescan

(b) SWFT of PE timescan
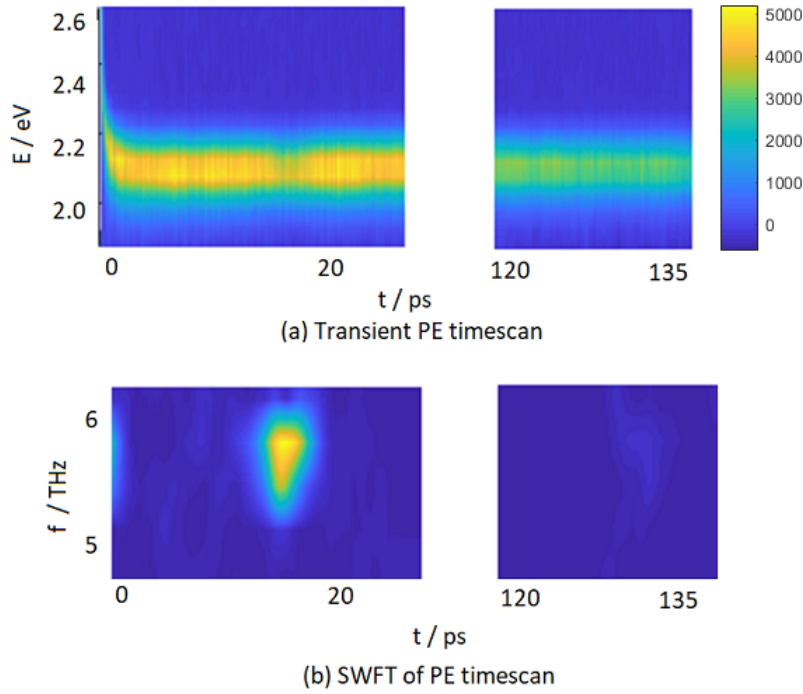
Figure 28: Determination of the oscillation period - PE timescan of the first 25 ps and the scan over the eighth revival with 319.9 nm pump and 264.2 nm probe wavelength. a.) PE timescan and b.) SWFT of the PE timescan - The loss in signal strength at the eigth revival can be accounted to a spacial loss of the overlap. (Lab.book:20.05.2021, timescan 194)
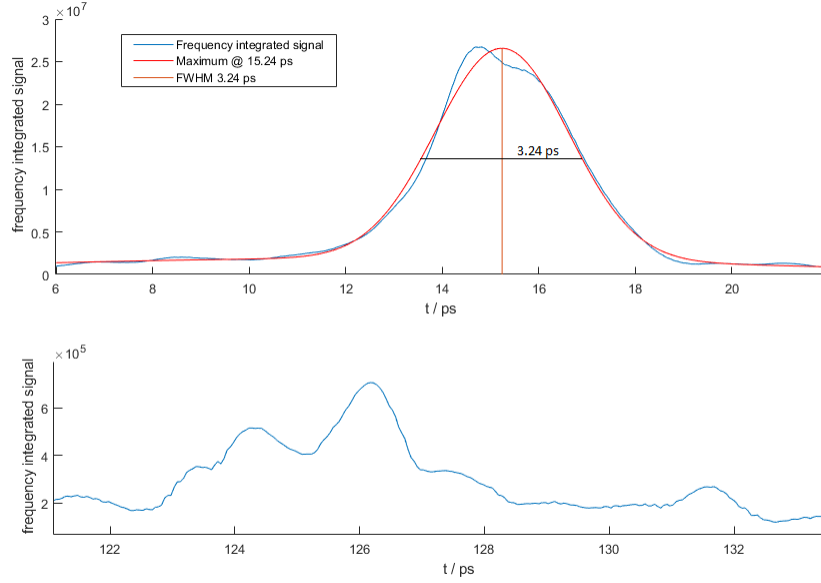
Figure 29: Determination of revival period - frequency integrated signal of SWFT for the determination of the oscillation period. The FWHM of the frequency integrated signal of the first revival is (3.2 ± 0.3) ps. The first revival has been determined at (15.2 ± 1.6) ps and the eighth revival at (126.2 ± 1.6) ps. (Lab.book:20.05.2021, timescan 194)

The first revival has been determined at (15.2 ± 1.6) ps and the eighth revival at (126.2 ± 1.6) ps within this measurement. The revival period τ_{rev} has been deduced to be:

$$\tau_{\mathrm{rev}} = (15.8 \pm 0.2) \text{ ps}$$

The lower oscillation shows also the same revival period. Since the scans of figure 28 have been made after each other, the weaker signal should not be related to a weaker OPA signal. The weaker signal at the eighth revival can be accounted to a spacial loss of the overlap.

The theoretical dispersion time of state E, which is the time after which the wave-packet should be completely dispersed, can be calculated with equation 12 from reference [15]:

$$\tau_{\mathrm{disp}} = \frac{h^2 * \nu}{(2 * \Delta E * \omega_e x_e)} = \frac{(4.1 * 10^{-15} eVs)^2 * 6 * 10^{12} s^{-1}}{2 * 0.05 eV * 0.00012 eV} = 8.5 \text{ ps}$$

We used the oscillation time of the gas-phase v=0 state of the E-state of $\nu = 6$ THz, the FWHM of the 319 nm excitation pulse of 0.05 eV as the energy difference ΔE and 0.00012 eV for the anharmonicity of the E-state. Since we can't detect when the dynamic has completely vanished, we take $\tau_{\mathrm{disp}}/2 = 4.25$ ps to compare it with the measured FWHM of the oscillation signal. We took the FWHM of the 319 nm excitation pulse of 0.05 eV for ΔE to define which states are

excited with the pulse. Since the pulse is effectively broader than the FWHM and also excites higher and lower states into our wave packet we can expect that the experimental dispersion time is shorter than this calculated value. The excitation of higher vibrational states then the v=0 state from the calculated value also results in a lower oscillation frequency and thereby shorter measured dipersion time than the calculated value. The mean measured FWHM of the frequency integrated signal from the SWFT of three revivals is (3.5 ± 0.3) ps. The measured and the theoretical values are compared in table 4. The theoretical dispersion time is 0.75 ps higher than the experimental measured dispersion time, as expected. Also with indium the theoretical dispersion time was 9 ps and the experimental (8 ± 1) ps.

3.1.4 Assignment of the Measured Parameters to the E-state

Figure 24 shows the potential energy curves for the electronic states of Al_2 and two ground states. The red area marks a reagion in which molecular dynamics are continuously observable, stemming from different states. The red line marks the E-state that has a theoretical dispersion time, oscillation period and revival time that can in very good agreement be ascribed to our experiments.

Table 3 shows the transition energies, the revival times and oscillation periods, energy differences between the transistion energies and the pump pulses, the hund's cases of several Al_2 states taken from reference [12] and of some $Al_2{}^+$ states from reference [13] and the pulse energy of used energie pulses. Although this are results from jet-cooled gas phase experiments, one can derive that we are examining the E-state of aluminium dimers. The lowest observable vertical ionization potential of the $X^3\Pi_u$ ground state is calculated and experimentally shown to occur around 6.1 eV. The dipole transition rule states, that we should only consider odd states for transitions since this is an even state. The lowest three possible ionisation states are listed in table 3 and need 6.6, 9.1 and 9.7 eV for the ionization. The PE energy of the lowest ionic state at 6.1 eV is displayed grey since the parities of the states should hinder the transition. Table 3 shows also the revival time and oscillation frequencies of the states that could be excited and lists the energetic mismatch to the states for gas phase transitions. The E-state would be excited 0.52 eV above the v=0 state in gas phase but the repulsive forces of the helium shifts the potential energy curves upwards and thereby reduce the ΔE_{pu} in the helium environment.

The results from jet-cooled gas phase experiments and our measurements are compared in table 4.

Table 3: Transition energies of Al_2 [12] and Al_2^+ [29] states from the ground state $X3\Pi_u$ and provided pump and probe energies. The PE energy of the lowest ionic state at 6.1 eV is displayed grey since the parities of the states should hinder the transition

T_0 ... energy of the $\nu = 0$ level of the given electronic state relative to the $\nu = 0$ level of the ground state $X3\Pi_u$

ΔE_{pu}... Energy difference between 318 nm pump energy and T_0 in gas phase

HC ... ascribed Hund's case

PE ... Photon energy

Transition	T_0 / eV	t_{Rev}/ps	f/THz	ΔE_{pu}/eV	HC	PE /eV
Al2$^+$ X2Σ^+_g	6.1					
Al2$^+$ A2Π_u	6.6					
Al2$^+$ C2Σ_u+	9.1					
Al2$^+$ D2Δ_u	9.7					
H'$^3\Sigma_g^-$	4.75	18	7.3	-0.85	a	
G$^3\Pi_{og}$	4.27	81	7.1	-0.37	a	
F 3$^3\Sigma_g^-$	4.04	29	6.3	-0.14	b	
F'	3.85	5.7	7.3	+0.05	b	
F"	3.79	333	3.9	+0.11	a	
E'$^3\Pi_g$	3.48	2.8	16.5	+0.42	a	
E 2$^3\Sigma_g^-$	3.38	33	6.0	+0.52	b	
OPA 318 nm						3.90
THG 269 nm						4.61
THG 264 nm						4.70
OPA + THG(269 nm)						8.51
OPA + SHG(402 nm)						6.98

Table 4: Comparison of the wavepacket oscillation freqency, revival period and dispersion time of the Al_2 E-state and measurement results. The measured second revival in the upper and lower He_N signal is ascribed to the first full revival.

Lit... Gas phase values according to references [12] and [15]

He_N-u ... He_N upper signal; He_N-l... He_N lower signal

ν_{wp}... Wavepacket oscillation freqency from SWFT (measurement nr. 55476);

τ_{1stRev} ... First full revival (measurement nr. 55476) $\tau_{rev}/2$ ... Dispersion time (measurement nr. 194)

	Lit.	He_N-u	He_N-l
ν_{wp} / THz	6.0 ± 0.1	5.73 ± 0.13	5.77 ± 0.08
τ_{1stRev} / ps	33.0 ± 0.3	31.6 ± 0.5	31.6 ± 0.5
$\tau_{disp}/2$ / ps	4.25	3.5 ± 0.3	-

Figure 30 shows the morse potentials of the states that are most likely involved whithin the excitation and ionization of Al_2 in this experiment. The state that has been assigned to be the groundstate of aluminium dimers is the $X^3\Pi_u$ state and due to the cooling of the helium

environment within our experiment, we assume that we are at this state before excitation. The excited state is most likely the E $2^3\Sigma_g$ state and the first ionic state that has a parity that allows a transition from this state is the $A^2\Pi_u$ state. With probe and pump wavelengths of about 269 nm (4.61 eV) and 318 nm (3.90 eV), like used in our experimental setting and dispicted in table 3, we arrive at a resulting energy of 8.51 eV. Since the lowest ionic state lies at 6.6 eV, the expected PE energy is 1.96 eV. The stronger upper state measured in this work lies at 2.1 eV, as shown in figure 27. The helium surrounding is pushing the gas phase PEC of the ground state and excited states upwards and lowers the ionic states. The difference in energy between the theoretical values and experimental values can hence be subscribed to a remaining influence of the helium surrounding or an excitation of an upper vibrational groundstate or ionization in an upper ionic state depending on the FC overlap.
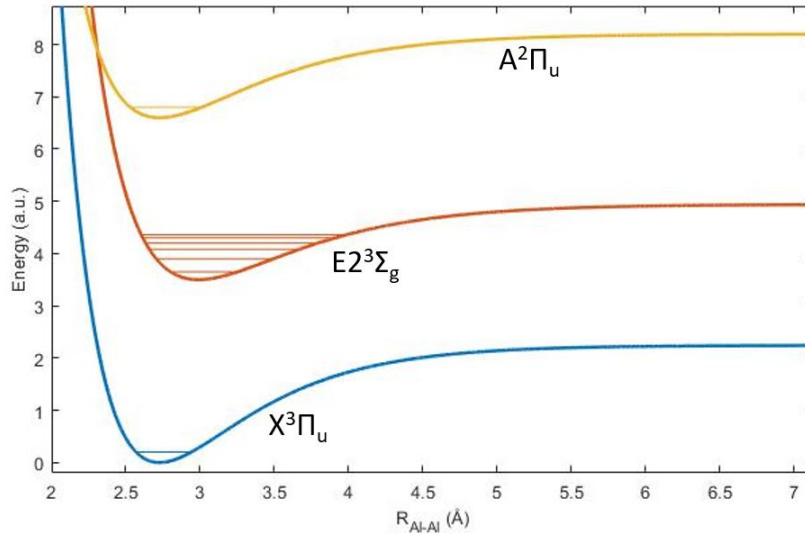
Figure 30: The morse potentials of the most likely involved states in the excitation and ionization of Al_2 in this experiment. The assigned ground state of aluminium dimers is the $X^3\Pi_u$ state which we assume to be populated due to the helium bath cooling. The excited state is most likely the E $2^3\Sigma_g$ state and the first ionic state that has a parity that is accessible from this state is the $A^2\Pi_u$ state. With probe and pump wavelengths of about 270 eV and 318 eV, like used in our experimental setting, the expected PE energy is 1.96 eV. The measured energy of the stronger state after the bubble expansion is 2.1 eV and the energy difference of the PEC can be subscribed to a remaining energy shift due to the helium environment.
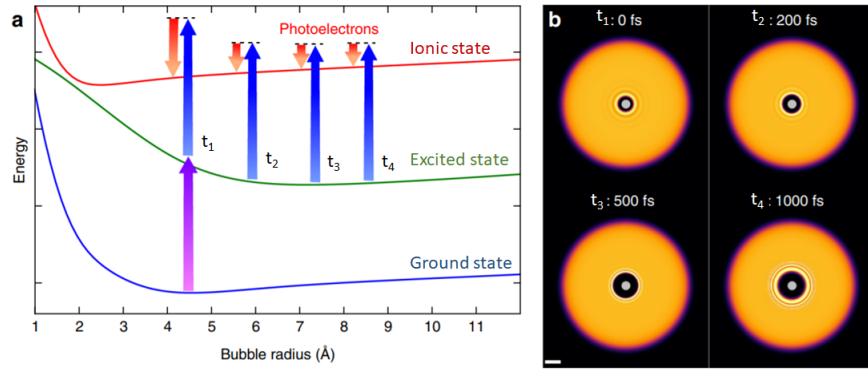
Figure 31: Schematic drawing of the temporal evolution of a doped He-system after photo-excitation. (a) Drawing of the potential energy curves as function of the bubble radius of a ground state, excited state and ionic state after excitation and ionization. The helium surrounding is suspected to shift the potential energy curve of the ground state and excited states upwards and lowers the ionic state PECs. After photo-ionization the radial distance increases and the effect of the helium decreases. This results in lower PE energies at later ionization times. (b) Simulation of the He-bubble expansion within the first 1000 fs for a He droplet with a single dopand. Altered figure from [15]

3.1.5 He-Bubble Expansion

Figure 31 shows the schematic drawing of the temporal evolution of a doped He-system after photo-excitation. One can see the potential energy curves as functions of the bubble radius of a ground state, excited state and ionic state after excitation and ionization. The helium surrounding is suspected to compress the potential energy curve of the excited state to higher lying energies with less radial distance. After photo-ionization the radial distance increases and the energy of the state drops. The process for ionic state is inverse due to attractive forces. This results in lower PE energies at later ionization times. Figure b shows a simulation of the He-bubble expansion within the first 1000 fs for a He droplet with a single dopand [15].

Figure 32 shows a PE transient timescan of the first few ps after excitation of aluminium dimers. There are two states observable. The upper state has a stronger signal than the lower state signal. In figure a one can see that, due to interaction with the helium surrounding, we get higher energetic photoelectrons. Within the first few ps after the excitation, the excited state PEC goes down again and the ionic state upwards since the helium bubble around the dopand expands [15]. Figure 32 b shows the energy integrated signal. At the pump probe overlap at t=0, the integration of the upper state signal is overlapping with a signal that goes into the probe pump direction, which is most likely stemming from another dopant like Al_3.

(a) PE timescan

(b) Integrated PE timescan
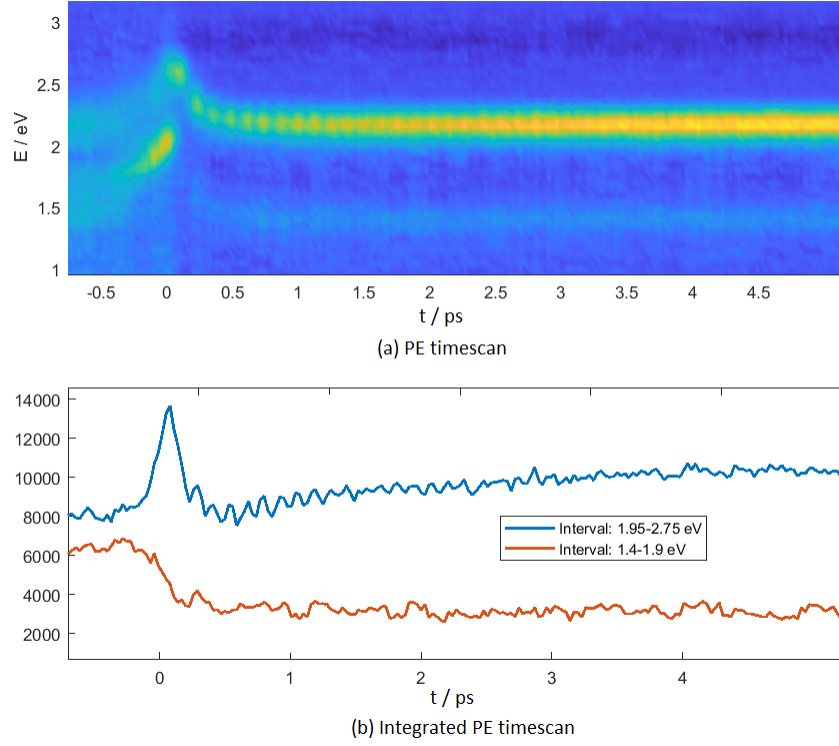
Figure 32: First 5 ps of a PE timescan with 319.9 nm excitation wavelength. (a) The PE timescan shows two states (b) The integrated signals for the two energy intervals of the states. The measurement has been done without calibration and has been energy corrected afterwards. (Lab.book: 01.12.2020)

The measurement with startnumber 57506, visible in figure 33, has been done calibrated. Therefore the fit parameters of the bubble expansion fit can be taken for further comparisons:

$$E_{\text{upper}}(t) = 0.44 \text{ eV} * \exp(-t/0.141 \text{ ps}) + 2.178 \text{ eV}$$
$$E_{\text{lower}}(t) = 0.44 \text{ eV} * \exp(-t/0.141 \text{ ps}) + 1.408 \text{ eV}$$

The energy difference between the two states is 0.77 eV. Since the coefficients of the not calibrated measurement visible in figure 34 are varying only slightly from the fit of figure 33, we can derive that the calibration we have done afterwards, by shifting the energy linearly to fit the calibrated measurement, can be done in this manner. The exponential decay of the fit in figure 35 is weaker than in the fit of figure 33. This can be ascribed to the poor energy resolution. The total shift is 0.4 eV for all measurements.
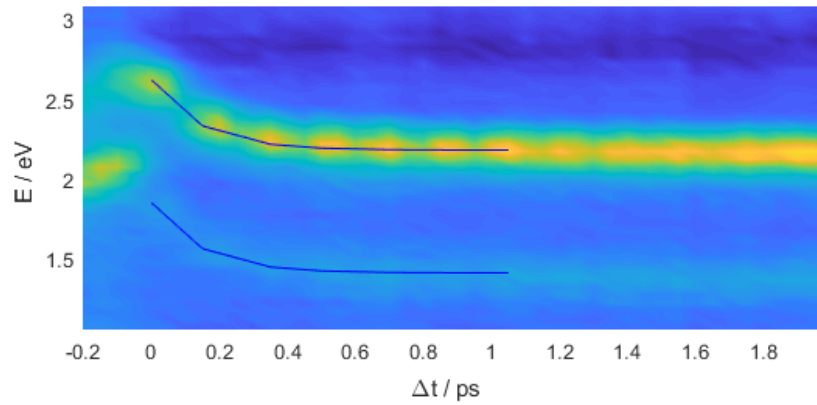
Figure 33: PE timescan of the bubble expansion and exponential fit of the upper molecular dynamics with the Al_2O_3 pots with 319.5 nm pump pulse and 269.6 nm probe pulse. The upper state starts at 2.55 ± 0.03 eV and drops to 2.15± 0.03 eV. The drop in signal of the upper oscillation is 0.4 eV. The start of the lower state is superimposed by another state most likely stemming from Al_3. This measurement has been done calibrated. Thereby the fit paramters of this fit can be taken for further comparisons. (Lab.book: 3.12.2021, eiTOF-start: 57506)
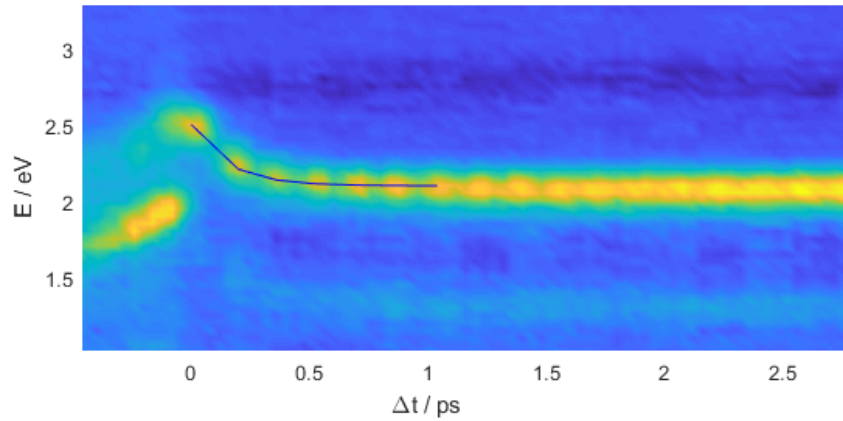
Figure 34: PE timescan of the bubble expansion and exponential fit of the upper molecular dynamics with the Al_2O_3 pots with 319.5 nm pump pulse and 269.6 nm probe pulse. This scan has been calibrated afterwards. The upper state starts at 2.55 ± 0.03 eV and drops to 2.15± 0.03 eV. The drop in signal of the upper oscillation is 0.4 eV. The start of the lower state is superimposed by another state most likely stemming from Al_3. Since the coefficients of the fit are varying only slightly from the fit of figure 33, we can derive that the calibration we have done afterwards by shifting the energy linearly to fit the calibrated measurement can be done. (Lab.book: 1.12.2021, eiTOF-start: 55476)
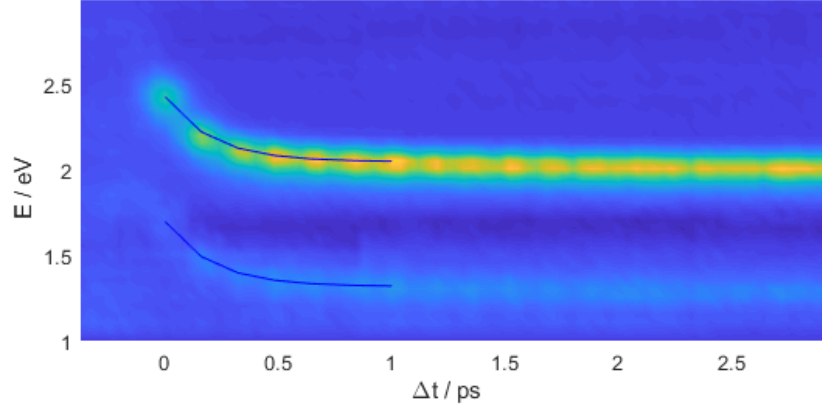
Figure 35: PE timescan of the bubble expansion of the second setup with BN-pots with 319.4 nm pump pulse and 264.2 nm probe pulse. The first strong original signal at the start of the lower stat is missing and the bleach is at a lower energy. The exponential decay in this fit is weaker than in the fit of figure 33. This can be ascribed to the energy resolution. The total shift is also 0.4 eV (Lab.book: 21.05.2021, timescan 203)

In Figures 33 and 34 a bleach is visible at (2.75 ± 0.03) eV, that is suspected to stem from a ground-state depopulation with the pump pulse.

The bubble expansion with the new BN-crucible setup is visible in figure 35. Since in figure 34 the lower signal is continuing on the probe pump side and not present in that direction in figure 35, the strong oscillation at the overlap of the lower signal in figure 34 is likely to stem from another dopand that is excitable with the 269.6 nm probe pulse. The bleach is in this setup at (1.75 ± 0.03) eV. Since it is not clear what the exact temperature of the different crucibles was, it is likely that the Al_2O_3 crucibles were heated more, making Al_3 a hot candidate for the additional dopant. With the BN crucibles the heating temperature might have been lower and the Al_3 content thereby much lower, giving no signal on the probe pump side. Figure 36 shows the energy shifts of the PE scans of the oscillation maxima from figure 35. The first signal of the lower state is also weakly visible and the energy shifts of both states are 0.4 eV.
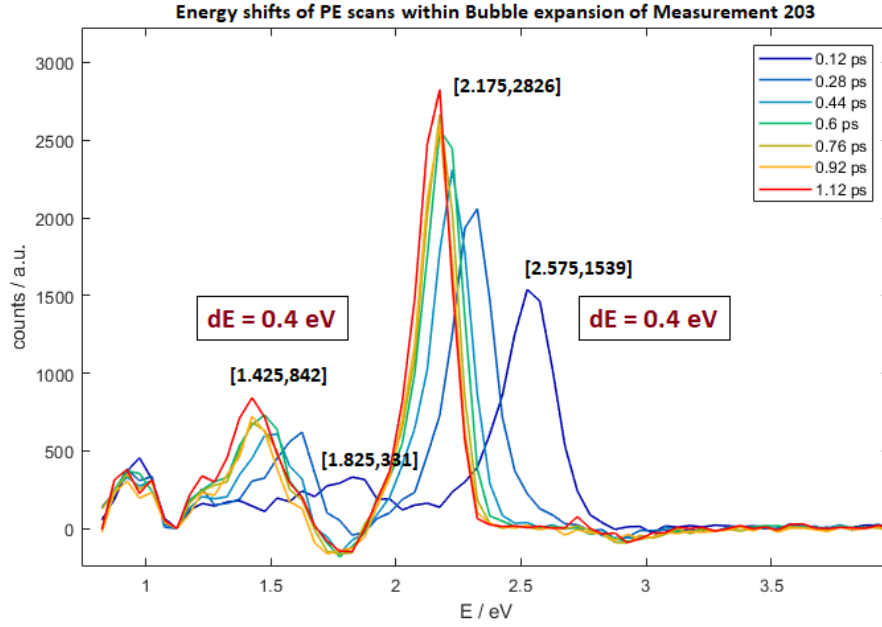
Figure 36: Energy shifts of PE scans within the bubble expansion with the BN-pot setup. The first signal of the lower state is weakly visible and the energy shifts of both states are 0.4 eV. (Lab.book: 21.05.2021, timescan 203)

3.1.6   Possible Scenarios Explaining Second Weaker State

It is not yet clear what causes the second signal that has the same oscillation frequency and revival period. The similarities speak for the same excited state. Figures 37 and 38 show two possible scenarios that could explain the second lower state, although the parity of the states should in theory not allow one transition in each scenario.

The first scenario of figure 37 states that a second state $d^1\Sigma_g{}^+$ 0.89 eV above the ground state, which is declared in reference [12], is also populated. This would give a PE signal with about 0.9 eV more, resulting in an additional signal with 2.9 eV. This value can vary depending on the equilibrium distance and the resulting FC overlap. The parity is even and would thereby in theory hinder the transition to the E $2^3\Sigma_g$ state. The lower state would have a merely higher oscillation frequency. Figure 27 shows that this might be the case, although the frequencies do not vary significantly.

The second scenario, described in figure 38, states that a second ionic state is also reachable. The $X^2\Sigma_g{}^+$ state, whos spectroscopic constants can be found in reference [13], has also even parity and thereby should theoretically not allow the transition. If the transistion would be

possible though and involve the lowest vibrational states in the ground and ionic state, the PEs in gas phase would have a PE energy of 2.5 eV. The measured PE energies before the bubble expansion match the PE energies of the second scenario. The equilibrium distance of the excited state is in the middle of the equilibrium distances of the higher ionic state $A^2\Pi_u$ and the lower ionic state $X^2\Sigma_g{}^+$ though. Since both PE signals have the same pattern, the Condon point has to be the same, what is not likely with two different ionic states that have different equilibrium positions.

Since we do not know how much the PECs of the ground state, the excited states and ionic states are shifted and how much energy is lost in the excited state shift of the bubble expansion, it is not possible to ascribe the energies so easily.

To summarize, the second weaker signal with 0.77 eV less energy is not yet explainable. Since the PE signals have the same pattern, what speaks for the same Condon point, a second ionic state is unlikely. The second ionic state would also have an energy difference of 0.5 eV instead of 0.77 eV. The second higher ground state would give PEs with additional 0.9 eV. Both scenarios also include a transition that violates the parity transition rules. Therefore neither of the scenarios is conclusive.
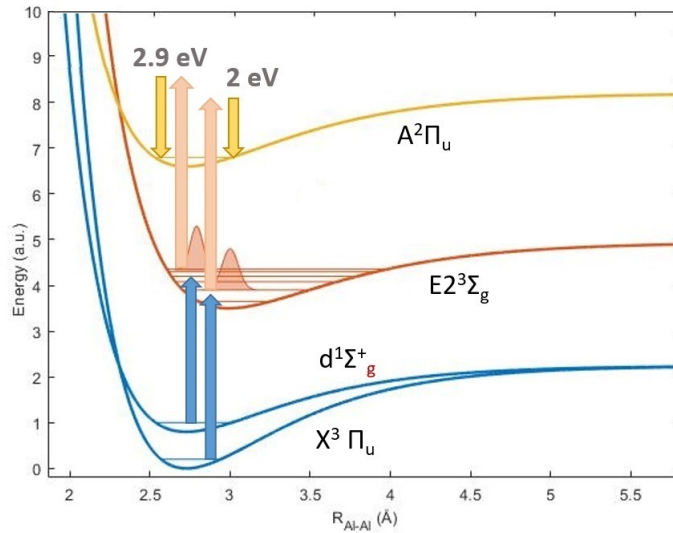
Figure 37: The first scenario states that a second ground state 0.89 eV above the original ground state is also populated. This would give a PE signal with 0.89 eV more, resulting in an additional signal with 2.89 eV. The parity is even and would thereby in theory hinder the transition to the E $2^3\Sigma_g$ state.
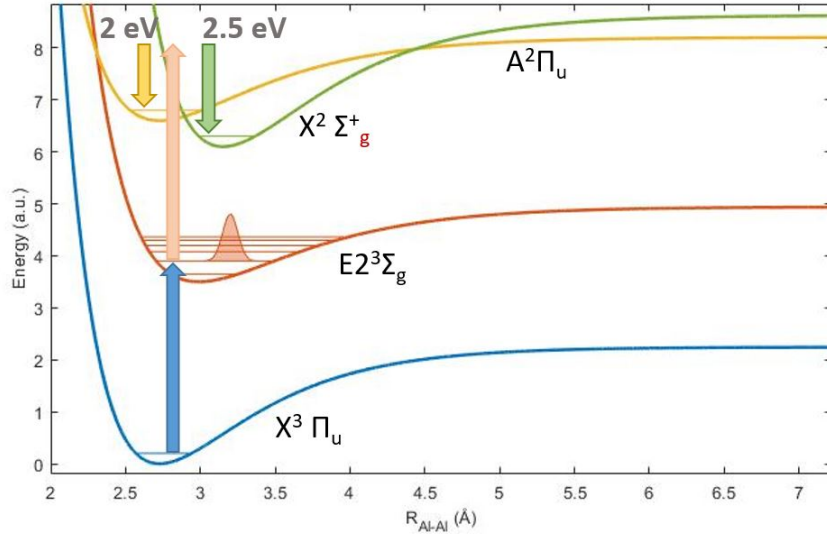
Figure 38: The second scenario states that a second ionic state. The $X^2\Sigma_g^+$ state has also even parity and thereby would not allow the transition in theory. In gas phase the additional PEs would have a PE energy of 2.5 eV which matches the energy before bubble expansion.

3.1.7 Revivals of aluminium dimers

As stated in the introduction, the anharmonicity of the harmonic oscillator leads to dispersion. Depending on the differences between the upper and lower spacings between the contributing states for the wavepacket, like stated in section 3.1, we obtain the revival times. At those time delays between pump and probe pulses the states of the wavepacket are in phase again and whenever there is a FC overlap with the ionizable state we get a strong PE signal. In figure 39 the PE timescan of the original oscillation and the first two revivals of a long time measurement are shown. Time windows of 6 ps have been chosen to investigate in the frequency domain how strong the oscillation contrast at each revival is. The whole measurement is shown in figure 40. The upper figures display the PE timescan and the lower figures show the energy integrated signals.
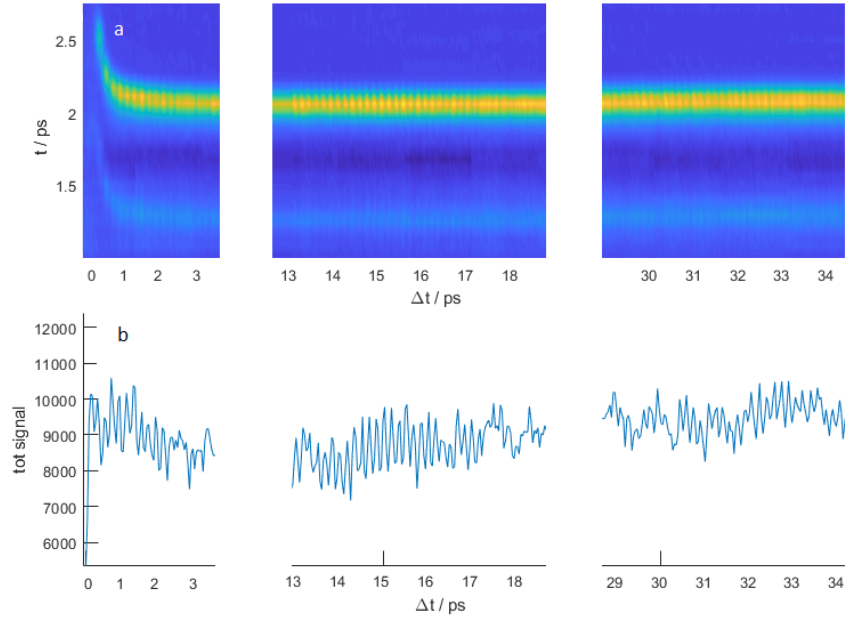
Figure 39: Original oscillations and two revivals of the transient PE spectrum and the associated integrated signal with 319.4 nm pump and 264.2 nm probe wavelength. a.) Transient PE timescan b.) Integrated PE timescan (Lab.book: 21.05.2021, timescan 203)
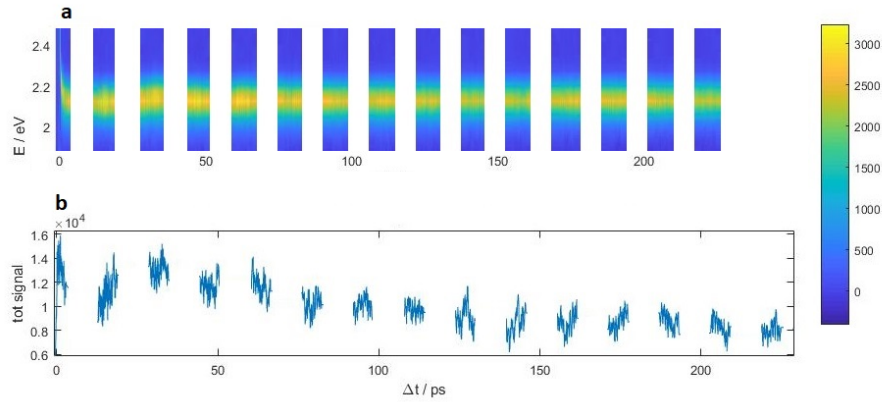
Figure 40: Long timescan of the transient PE spectrum and associated integrated signal with 319.4 nm pump and 264.2 nm probe wavelength. a.) Transient PE timescan b.) Integrated PE timescan (Lab.book: 21.05.2021, timescan 203)

Figures 41 and 42 show the sinusoidal fits of the wavepacket oscillations at 2.12 eV from the first revival up to revival eleven. The 8th, 9th, 10th, and 11th revivals were detrendend by substracting fitted sinusoidal functions. A sinusoidal fit was accepted when it gives a frequency

between 3.5 and 7.5 THz. The analysis obtained frequencies in the range of 5.75 to 5.89 THz for ten of twelve revivals of the measurement number 203.
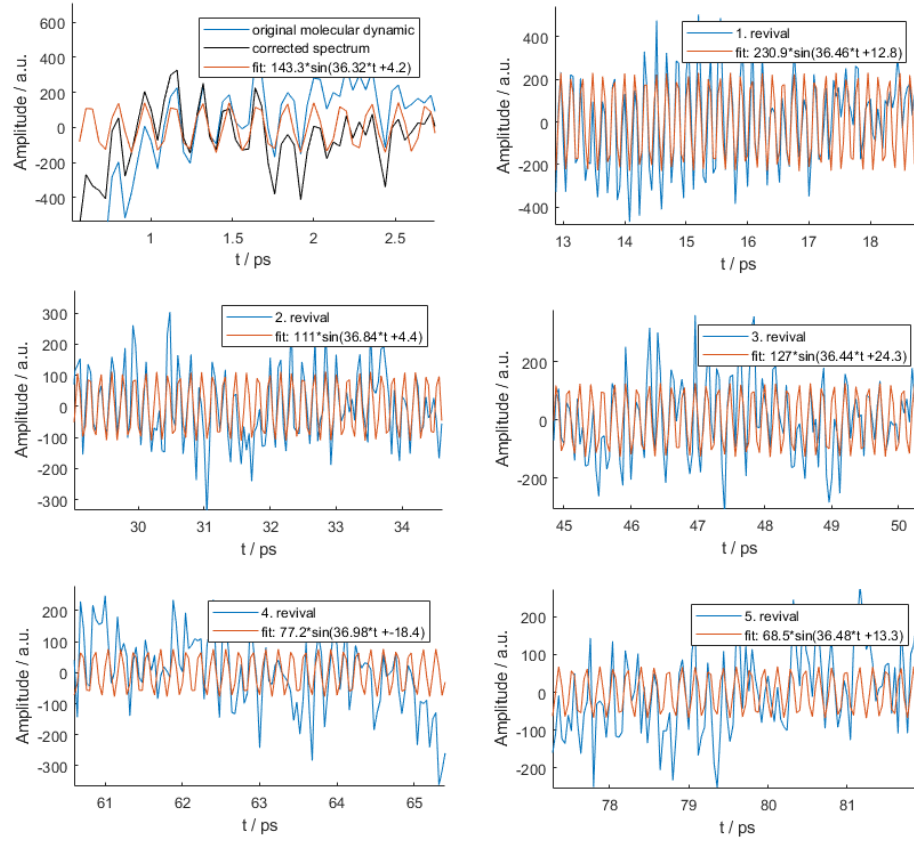
Figure 41: Sinusoidal fit of the first six wavepaket oscillations at 2.12 eV - The first revival has a circular frequency of 36.46 corresponding to a frequency of 5.80 THz. (Lab.book: 21.05.2021, timescan 203)
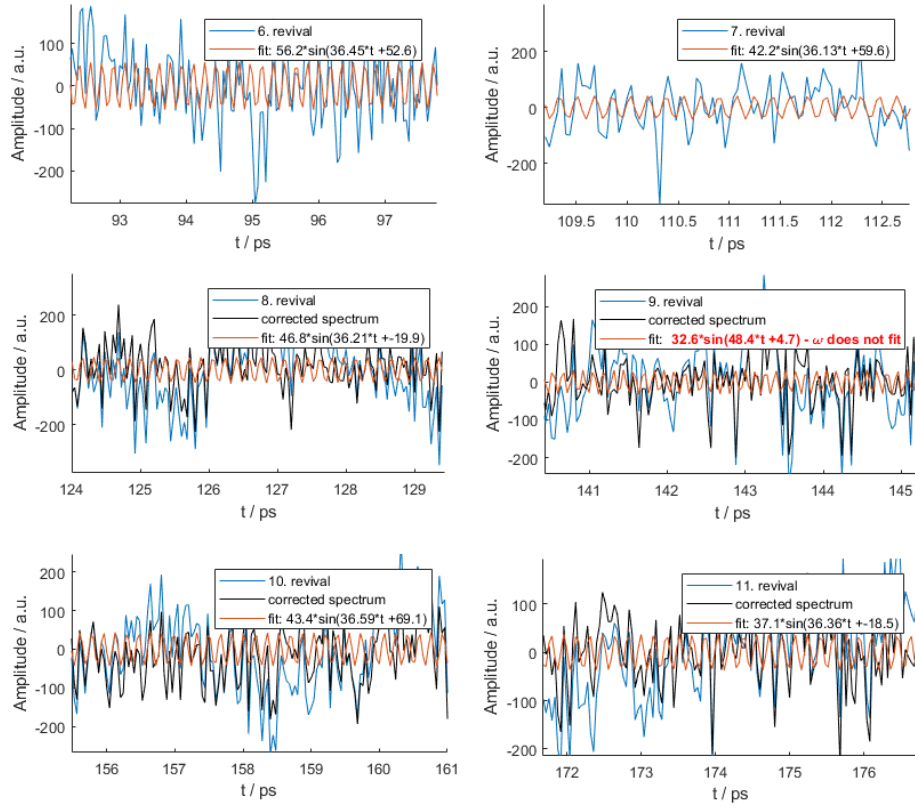
Figure 42: Sinusoidal fit of the seventh up to the eleventh revival at 2.12 eV (Lab.book: 21.05.2021, timescan 203)

The 9th and 12th revival could not be fitted and were excluded from the figures 44 and 43 in which the amplitudes and frequencies of the oscillation at each revival are shown.
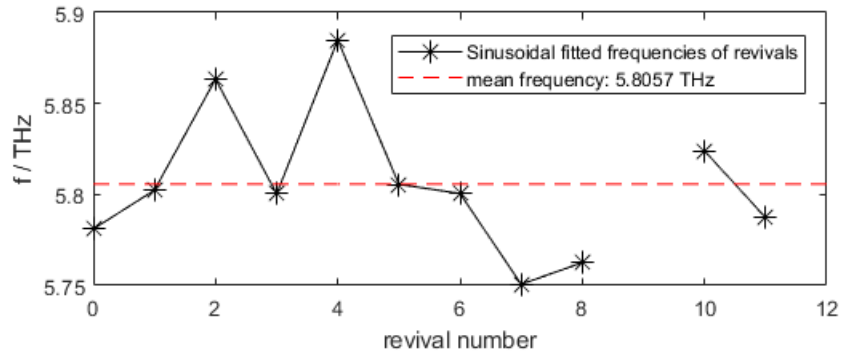
Figure 43: Frequencies of the sinusoidal fitted revival oscillations at 2.1 eV- The mean frequency is 5.81 THz. (Lab.book: 21.05.2021, timescan 203)

The mean wavepacket frequency of measurement number 203 is 5.81 THz. Figure 44 shows that the amplitude at the second revival is smaller than at the third revival. The frequencies at the revivals shows an oscillating trend whereby the second and fourth revival have higher frequencies than the other revival times.
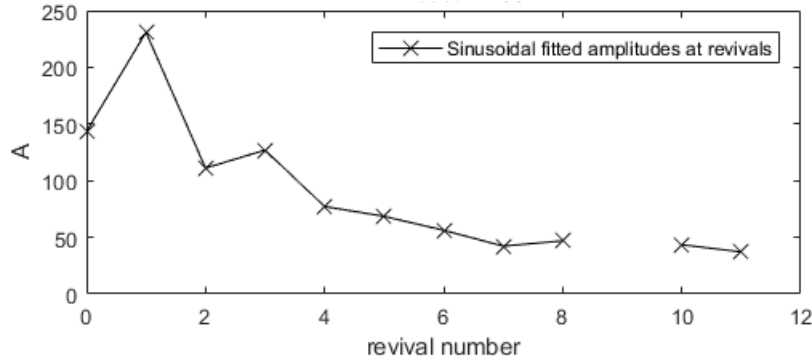
Figure 44: Amplidudes of the sinusoidal fitted revival oscillations (Lab.book: 21.05.2021, timescan 203)

The SWFT of the whole measurement gave a center frequency of (5.8 ± 0.2) THz. In figure 45 the frequency integrated signal from 5.5 THz to 6 THz is plotted over time to get an idea how fast the signal strength is dropping within the revival times. One can see double peaks in the second and fourth revival and that the first revival is stronger than the original signal. The second observation might be due to the helium oscillation. In three out of four scans, 203, 205 and 208, the oscillation strength of the second revival is stronger than the third revival. The scan 207, in which this was not observable, had a very fast dropping signal which made it not representative. Within the first six revivals one can see the tendency that the odd revivals are stronger than the even revivals.
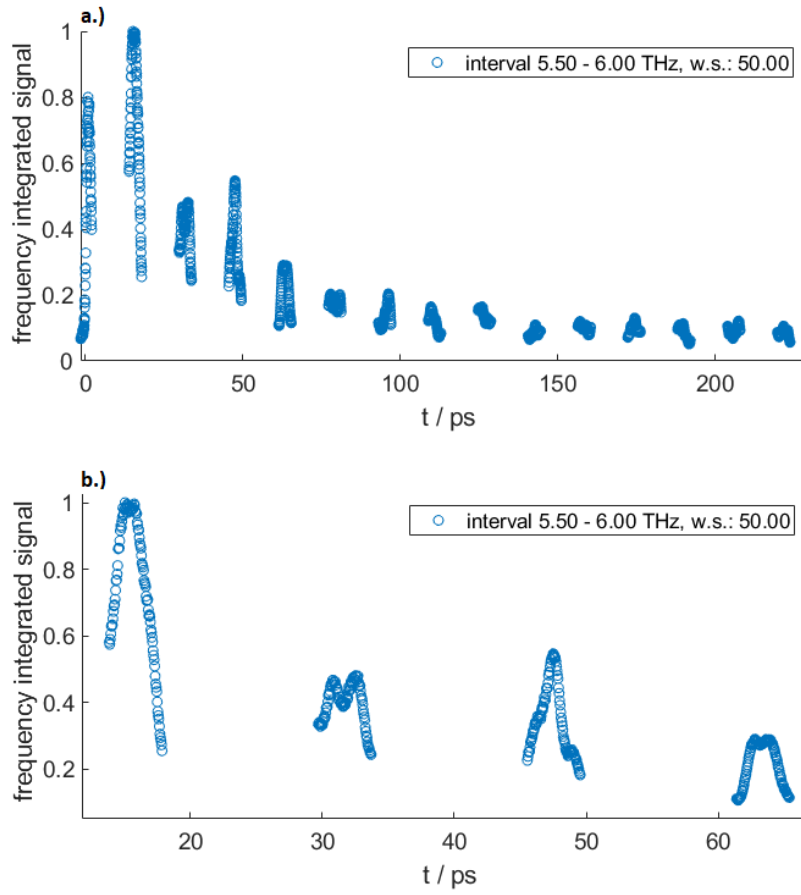
Figure 45: Frequency integrated SWFT of transient PE spectrum with 319.4 nm pump and 264.2 nm probe wavelength. A window size of 50 points was used. a.) Whole timeseries b.) Evaluation of the first four revivals - One can see double peaks in the second and fourth revival. The revival duration of the first four peaks is (3.2 ± 0.4) ps (Lab.book: 21.05.2021, timescan 203)]

Figure 46 a shows the frequency components of the PE timescan signals of each revival. The Fourier transformation for this analysis used the SWFT method with a window size that includes the whole revival window of 6 ps. The red area marks the frequency range which was integrated on the time scale in figure 45. In the inset, the integrated signals at later revival times are shown. Figure 46 b shows the oscillation amplitude in the frequency domain as the signal to noise ratio of the signals with frequencies between 5.5 THz and 6 THz to the background, for which the mean signal of all recorded frequencies has been used. The amplitude in the time domain, which was displayed in figure 44, is plotted above to visualize that the courses are similar. The oscillation amplitude in the time domain has been normalized to make the first revivals have the same height for comparison. One can see how fast the oscillation contrast drops at higher time delays. At 111 ± 3 ps time delay the ratio between the frequency domain

signal at the oscillation frequency of the molecular dynamics and the mean signal strength is already 1.3. At 127 ± 3 ps we have a ratio of 1.5 again. At the ninth and twelfth revival the signals were the lowest with 1.1 and 1 and at this revivals it was also not possible to fit a sine function to the signal in the time domain, although it was possible to fit a sinusoidal function at the twelfth revival in two of the other scans at this revivals.
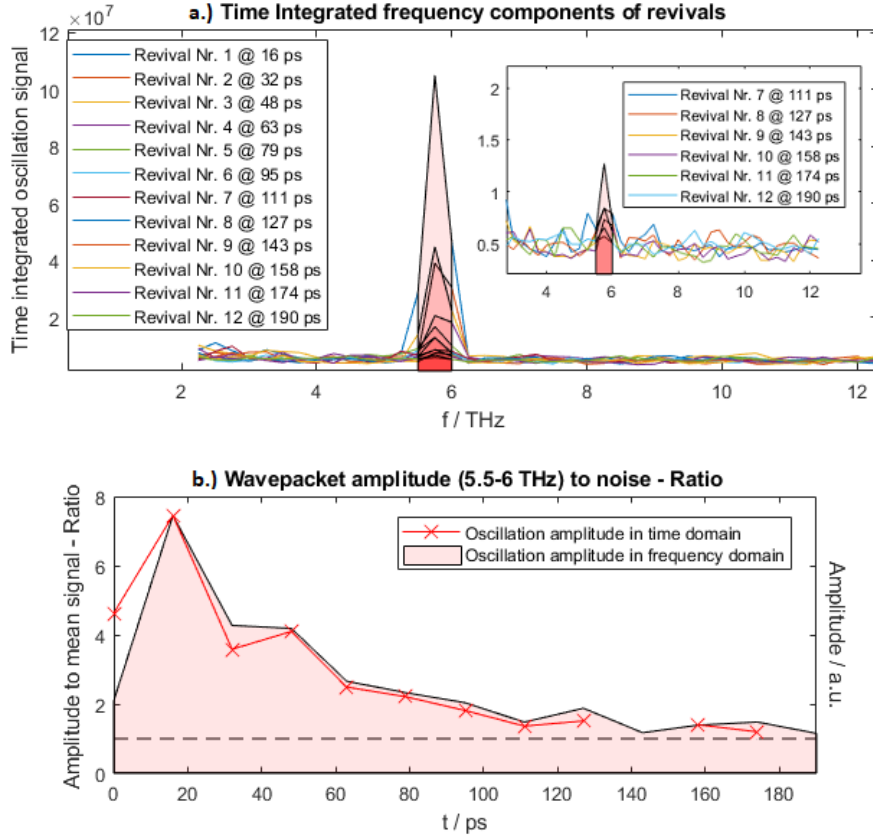
Figure 46: Fourier transformation of the transient PE spectrum with 319.4 nm pump and 264.2 nm probe wavelength of original oscillation and revivals. a.) Frequency components of the PE timescan signals of each revival. The red area marks the frequency range which was integrated for the oscillation amplitude in the frequency domain. b.) The oscillation amplitude in the frequency domain: The signal to noise ratio of the signals with frequencies between 5.5 THz and 6 THz to the background, for which the mean signal has been used. The oscillation amplitude in the time domain: The amplitudes of the sinusoidal fits for the original oscillation and the revivals. For normalization the time domain oscillation amplitudes have been scaled to the frequency domain to make the first revival signals equal in height. (Lab.book: 21.05.2021, timescan 203)

The figures 47 and 48 show the amplitudes and frequencies of the three most useful scans. One can see an oscillating behaviour between the revivals that is inverse for amplitudes and frequencies. This oscillation could be due to a helium bubble oscillation which could lead to a compression of the potential energy curves. Energy conservation would also demand higher

amplitudes at lower frequencies and vice versa which makes this behaviour plausible.   The
obtained oscillation frequency is:

$$\nu = (5.81 \pm 0.02) \text{ THz}$$

Whereby the uncertainty of 0.02 THz stems from the scattering of the measurement frequencies
at each revival, that vary to up to 0.2 THz. This would explains a high uncertainty of the
oscillation frequency of a whole measurement series, like depicted in figure 26. Although the
short measurement windows of 6 ps also limit the frequency resolution.

In the frequency domain, like visible in figure 46, it is not clear if the oscillation is still ob-
servable after 111 ps. In the time domain, like displayed in figure 43, the sinusoidal fit gave
oscillations in the range of 5.75 and 5.89 up to 200 ps. This shows an overall trend that the
oscillation amplitude stays constant after 111 ps. Nevertheless with some of the revivals a fit
was not possible.

Since the frequencies are not increasing at higher time delays, dissipation by relaxation in lower
lying states, due to interaction with the helium or other dopants, is not likely. The total counts
are decreasing from 14000 to 8000, as displayed in figure 40, implying a sufficiently good spacial
overlap at higher delays. The reason for the nevertheless fast decaying signal contrast is not
clear yet.
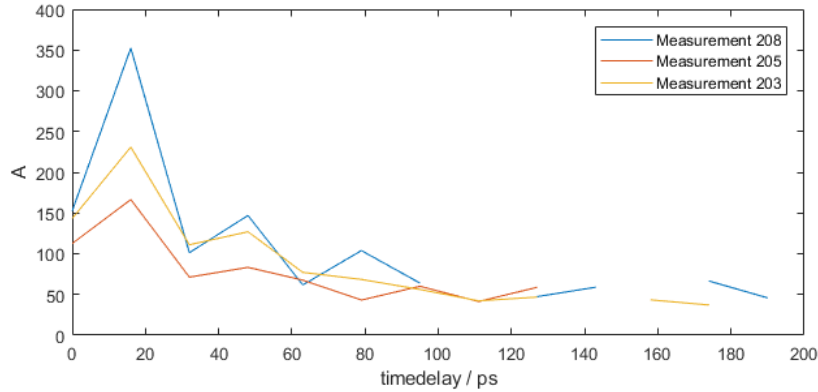
Figure 47: Amplitudes of the sinusoidal fitted revival oscillations of three measurements with BN-crucibles
(Lab.book: 21.05.2021, timescan 203, 205, 208)
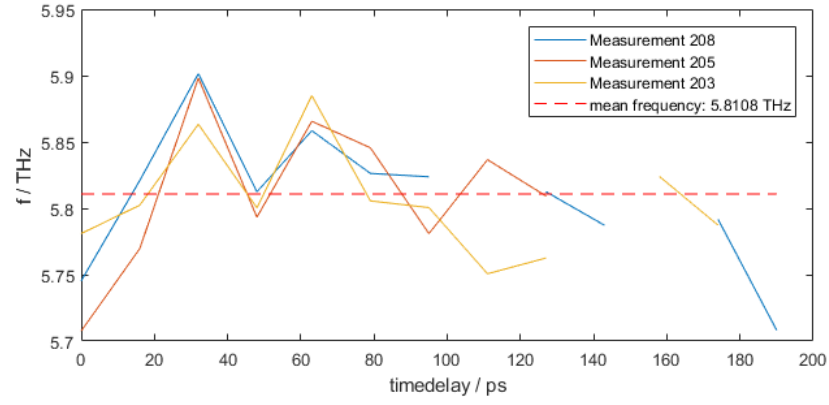
Figure 48: Frequencies of the sinusoidal fitted revival oscillations at 2.1 eV of three measurements with BN-crucibles - The mean frequency is 5.81 THz. (Lab.book: 21.05.2021, timescan 203, 205, 208)

3.2 Further Results

In the following additional measurements and their results are shown.

3.2.1 Al$_2$O$_3$ Crucible Setup - 315 nm Pump and THG Probing

In figure 49 the transient PE spectrum of the first 4 ps with 315.1 nm pump wavelength and 296.6 nm probe wavelength and the energy integrated signal over all energies is shown. The occurring 0.45 eV PE energy shift is 0.05 eV more than within the measurements with 319.5 and 319.4 nm probe wavelength where both times an energy shift of 0.4 eV occured. This states, that higher vibrational states experience a stronger energy shift.
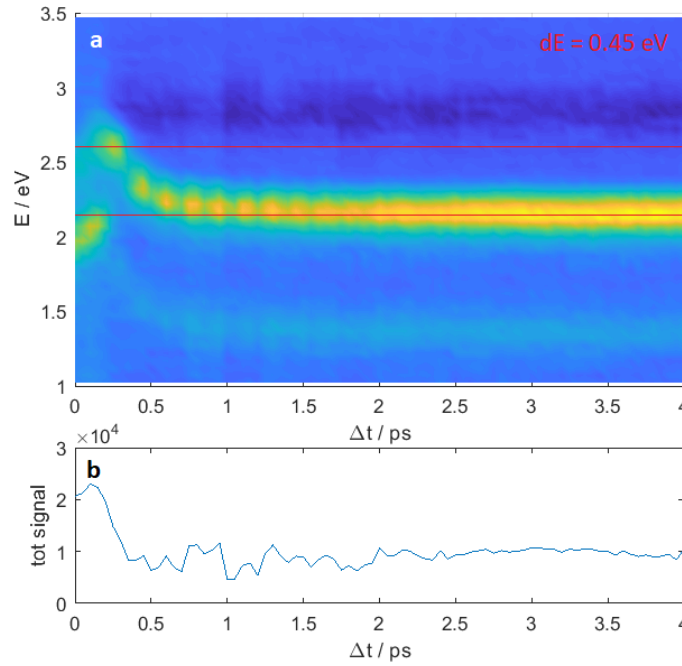
Figure 49: Transient PE spectrum within the first 4 ps with 315.1 nm pump wavelength and 296.6 nm probe wavelength. (Lab.book: 03.12.2020)

The SWFT of this measurement is visible in figure 50. The evalutation of the first revival is visible and gives an oscillation frequency of (5.67 ± 0.15) THz.
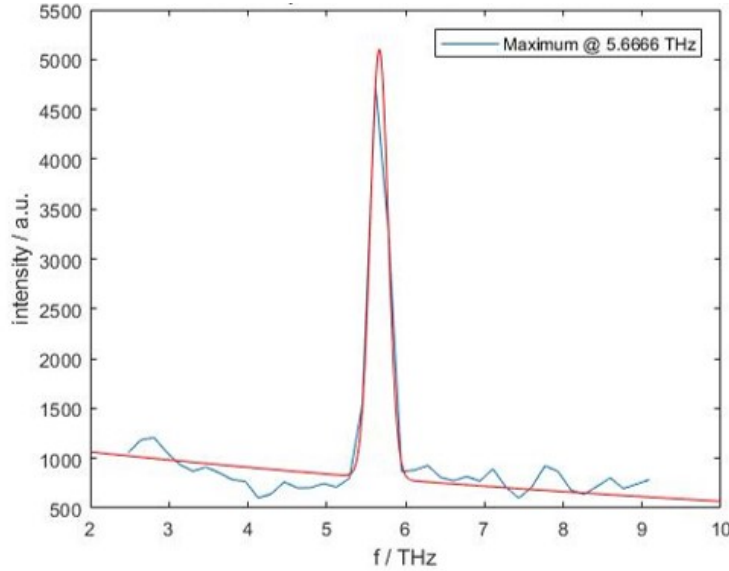
Figure 50: The SWFT of the first revival with 315.1 nm pump pulse and 296.6 nm probe wavelength gives an oscillation frequency of (5.67 ± 0.15) THz. (Lab.book: 03.12.2020)

By comparing the two stronger states with 315.1 nm and 319.5 nm, from figure 27 and 50 respectively, we see, that we get a lower oscillation frequency of (5.67 ± 0.15) THz at 315.1 nm in comparison with the (5.73 ± 0.13) THz at 319.5 nm. That is consistent with the expectation, that higher energy pulses can excite higher lying vibrational states, that have a higher range of movement within the potential energy well and thereby a lower frequency. This also fits to the v_0 state in gas phase from the literature [12] that has an oscillation frequency of (6.0 ± 0.1) THz.

3.2.2   BN Crucible-Setup - 319.3 nm and 319.4 nm Pump and 264.2 Probing

Due to the high reactivity of Al with Al_2O_3 crucibles, the second measurement series was conducted with BN crucibles and a tantal shield.

Figures 51 - 57 show another three timescans with 319.3 nm and 319.4 nm pump wavelength. For timescan 205 the PE timescan and the integrated signal of the SWFT from 5.5 to 6 THz, to display the rising and falling oscillation strengths within each revival, are shown in 51 a and b. In figure 52 a the frequency components of the oscillation from the Fourier transformation of each revival are displayed. Figure 52 b shows again the amplitudes of the oscillation strength between 5.5 and 6 THz as the oscillation amplitude in frequency domain and the amplitudes of the sinusoidal fits as the oscillation amplitudes in time domain. One can, also for this scan, see, that the course of the amplitudes of the Fourier Transformation is matching the course of the

amplitudes of the sinusoidal fits. It is notable that the second revival at 32 ps, that corresponds to the first full revival of the E-state shows a lower oscillation amplitude in the scans 203, 205 and 208 than the first and third measured revival, corresponding to a lower oscillation contrast at the full revival. One can also see in this timescans, that the oscillation amplitudes of the first five revivals show an oscillating behaviour again.
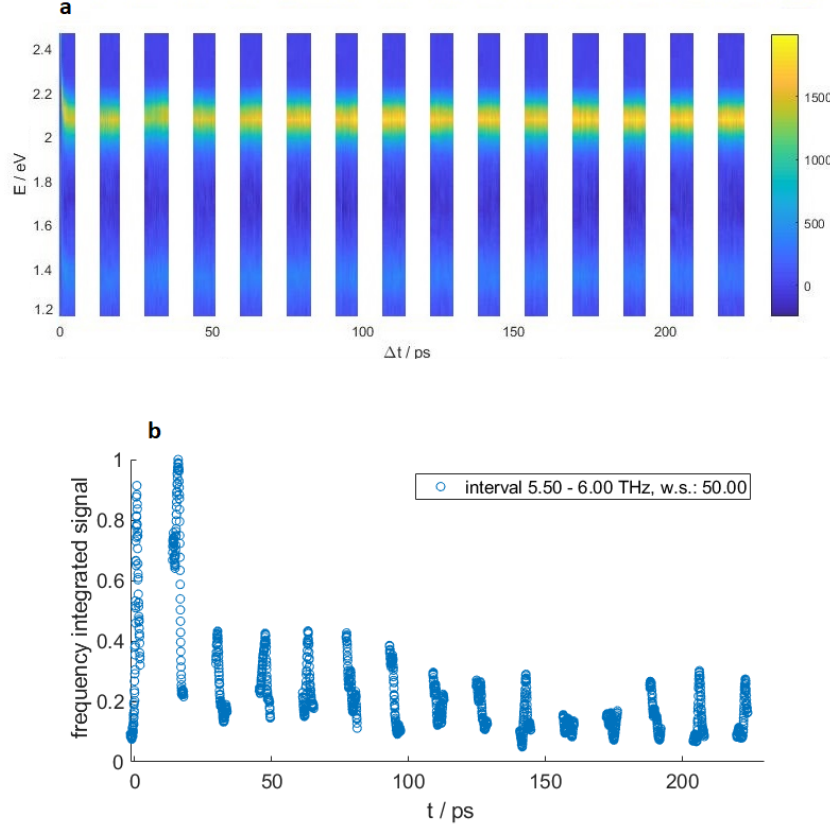
Figure 51: Evaluation of timescan 205 with 319.4 nm pump and 264.2 nm probe wavelength: a.) Transient PE spectrum b.) Frequency integrated signal to determine the rising and falling of the oscillation amplitude within each revival (Lab.book: 21.05.2021, timescan 205)
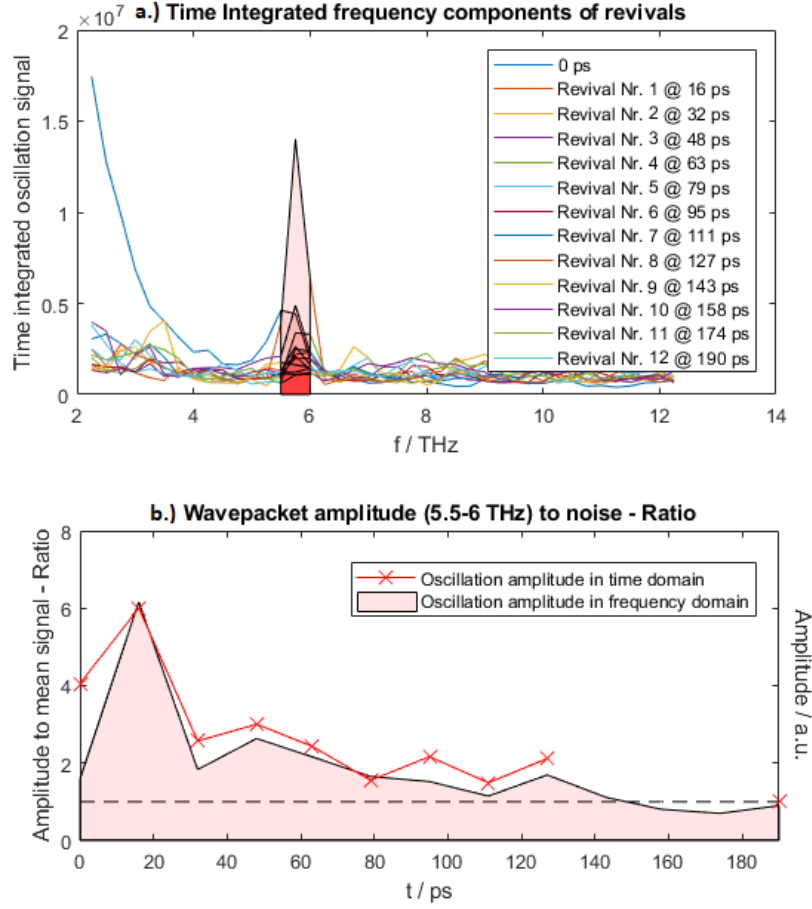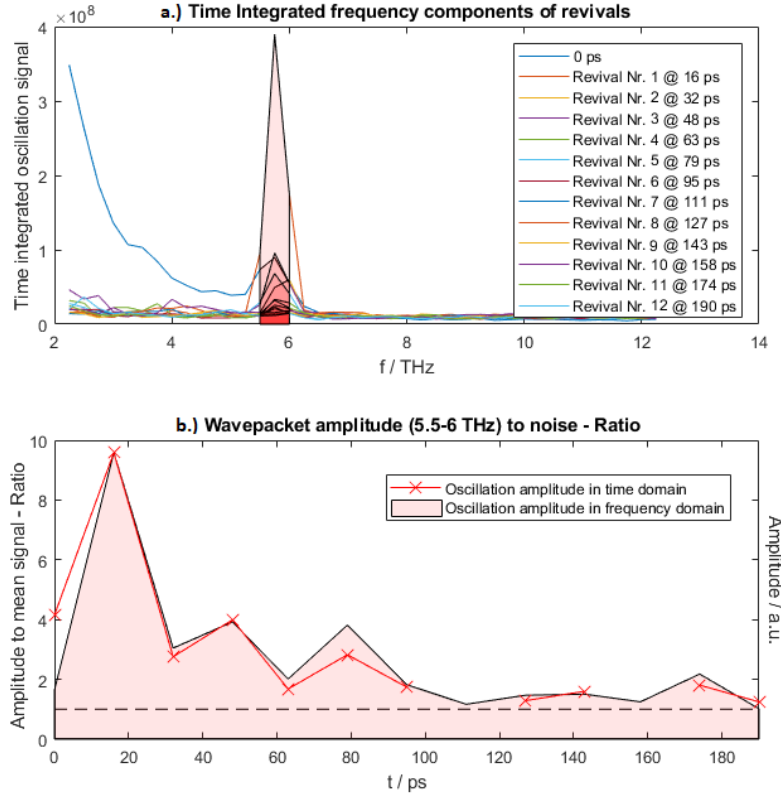
Figure 52: Fourier transformation of the transient PE spectrum with 319.4 nm pump and 264.2 nm probe wavelength of original oscillation and revivals. a.) Frequency components of the PE timescan signals of each revival. The red area marks the frequency range which was integrated for the oscillation amplitude in the frequency domain. b.) The oscillation amplitude in the frequency domain: The signal to noise ratio of the signals with frequencies between 5.5 THz and 6 THz to the background, for which the mean signal has been used. The oscillation amplitude in the time domain: The amplitudes of the sinusoidal fits for the original oscillation and the revivals. For normalization the time domain oscillation amplitudes have been scaled to the frequency domain to make the first revival signals equal in height. (Lab.book: 21.05.2021, timescan 205)

Figure 53: Evaluation of timescan 207 with 319.4 nm pump and 264.2 nm probe wavelength: a.) Transient PE spectrum b.) Frequency integrated signal to determine the rising and falling of the oscillation amplitude within each revival (Lab.book: 21.05.2021, timescan 207)
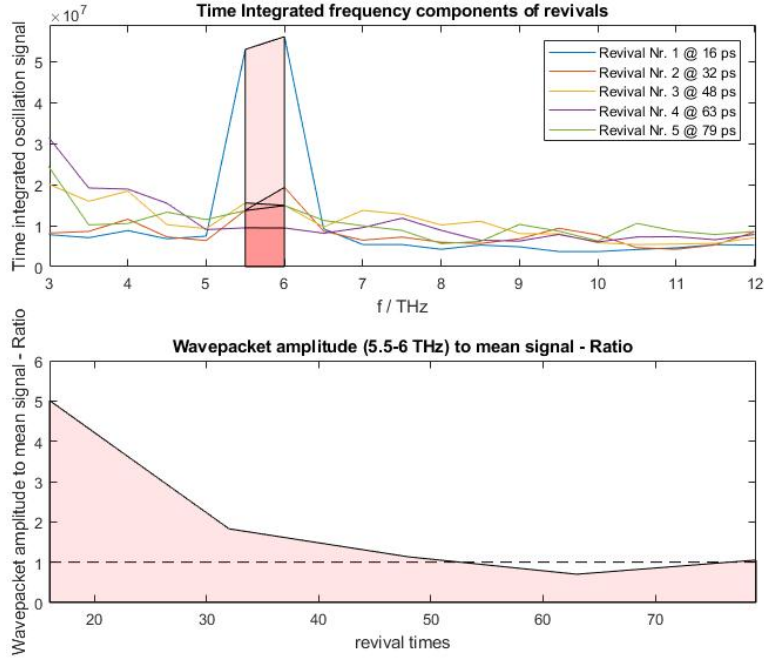
Figure 54: Fourier transformation of the transient PE spectrum with 319.4 nm pump and 264.2 nm probe wavelength of original oscillation and revivals. a.) Frequency components of the PE timescan signals of each revival. The red area marks the frequency range which was integrated for the oscillation amplitude in the frequency domain. b.) The signal to noise ratio of the signals with frequencies between 5.5 THz and 6 THz to the background, for which the mean signal has been used. (Lab.book: 21.05.2021, timescan 207)

Since the timescan 207 is shorter and had less good resolution than the other scans in that measuring period it has not been included in the figures 47 and 48, that show the courses of the amplitudes and frequencies in the time domain. Therefore they are displayed in figure 55 and figure 56.
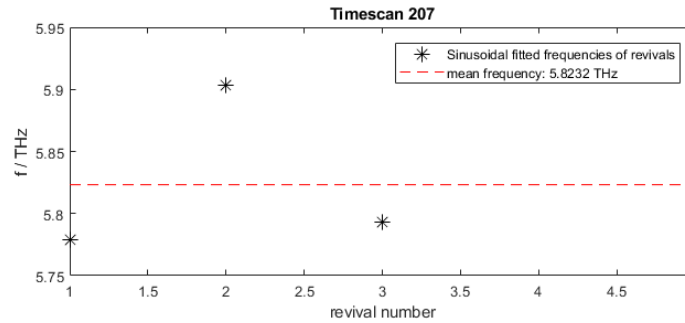
Figure 55: Frequencies of the sinusoidal fitted revival oscillations at 2.1 eV - The mean frequency is 5.82 THz. (Lab.book: 21.05.2021, timescan 207)
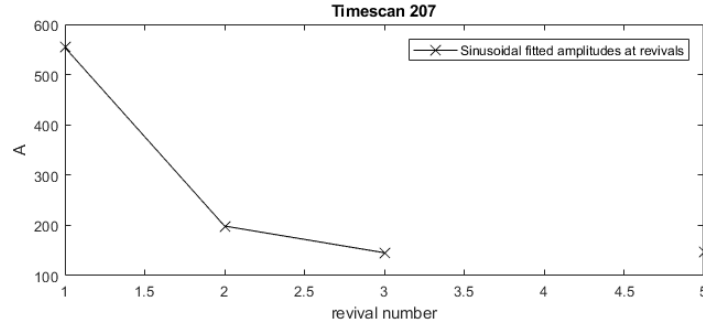
Figure 56: Amplitudes of the sinusoidal fitted revival oscillations at 2.1 eV (Lab.book: 21.05.2021, timescan 207)
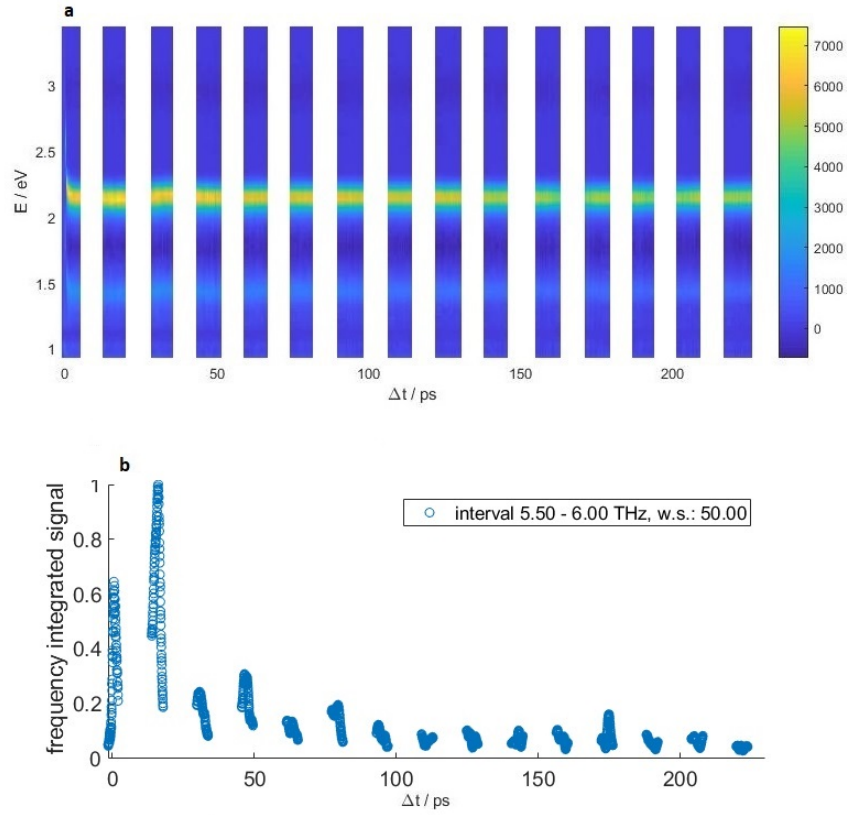
Figure 57: Evaluation of timescan 205 with 319.3 nm pump and 264.2 nm probe wavelength: a.) Transient PE spectrum b.) Frequency integrated signal to determine the rising and falling of the oscillation amplitude within each revival (Lab.book: 21.05.2021, timescan 208)

Figure 58: Fourier transformation of the transient PE spectrum with 319.3 nm pump and 264.2 nm probe wavelength of original oscillation and revivals. a.) Frequency components of the PE timescan signals of each revival. The red area marks the frequency range which was integrated for the oscillation amplitude in the frequency domain. b.) The oscillation amplitude in the frequency domain: The signal to noise ratio of the signals with frequencies between 5.5 THz and 6 THz to the background, for which the mean signal has been used. The oscillation amplitude in the time domain: The amplitudes of the sinusoidal fits for the original oscillation and the revivals. For normalization the time domain oscillation amplitudes have been scaled to the frequency domain to make the first revival signals equal in height. (Lab.book: 21.05.2021, timescan 208)

The best resolution was obtained with scan 203. Although the signal in frequency domain is already very weak after the seventh revival, one can observe within the scans 203 and 208 that the oscillation amplitude is not completely vanishing and is staying constant after 111 ps, although the sinusoidal fit could not be obtained with all scans. Within the scan 205 a higher sampling rate window of 1 ps within the scanning window of 6 ps was added and neither the OPA, nor the overlap was optimized. The higher sampling rate of 0.01 ps instead of 0.04 ps did not improve the resolution, indicating that the stage has reached its limit in position accuracy. For timescan 207 the overlap was optimized and for timescan 208 also the OPA was optimized. There was a progressing destruction of the tungsten basket holders due to the reaction with the

aluminium over these timescans. The ongoing dissolving of the tungsten wires is dispicted in figure 14. This could have lead to the worsening of the resolution. The QMS displayed although that the signals of He, Al and Al_2 stayed constant over this measuring period.

3.2.3   SHG Measurements

Within measurements with Second Harmonic Generation (SHG) instead of THG there was a strong state in the region of the bleach visible with no bubble expansion and dynamic, as visible in figure 59. The dynamic in the state with the bubble expansion is very weak. There are also some weak oscillations visible around 3 eV and 5 eV which might stem from multi-photon ionization. The sliding window Fourier analysis does show only a very weak oscillation with 6 THz, as visible in figure 60. This is 0.27 THz higher than with THG probing. Figure 59 shows that the lower signal looses its strength quite fast and the state at 2.18 eV seems to get populated after the first oscillation of the lower state what is not explainable.
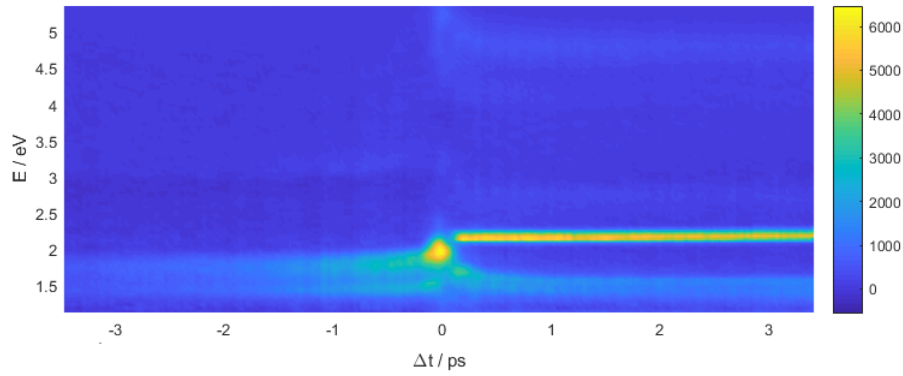
Figure 59: Transient PE spectrum with 317.8 nm pump wavelength and 402.5 nm probe wavelenght - calibrated according to similar measurement with another repeller voltage (0.2 BBO SHG) (Lab.book: 30.11.2020)
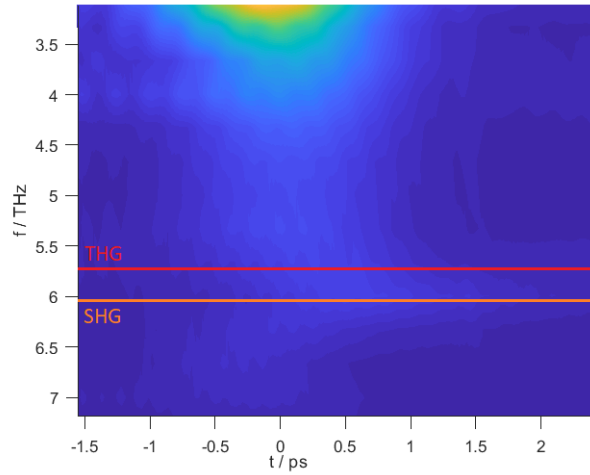
Figure 60: SWFT of the transient PE spectrum with SHG probing - SWFT just gives very weak indication for oscillation after 317.8 nm pump wavelength and SHG probing with 402.5 nm wavelength. The frequency of (6.0 ± 0.2) THz is also higher than the frequency measured with 319.5 nm pump wavelength and THG probing. (Lab.book: 30.11.2020)

3.2.4   Dimer Ejection

After photo excitation of dopants in helium droplets, with some dopants it has been observed that they are pushed out of the droplet. In our research group this observation has been made with indium [15]. In a previous photodissociation experiment of our group on Cr_2 inside He_N it was observed that Cr fragments were not ejected from the droplet, in spite of 0.4 eV excess energy freed in the dissociation process [30]. Complete trapping of fragments was also reported for NO_2 inside He_N [31].

Aluminium dimers have been observed to get ejected and the detected ions show a similar behaviour as observed with indium. An ionisation shortly after the excitation, when the dimer is still within the droplet, leads to an attraction and capturing of the ion in the helium droplet. This leads to the conclusion that a rise in mass signal is showing the increase of ejected dimers of this mass. Figure 61 shows the time scan of the ion yield signals that displays a rise in mass 54 and thereby a rise in Al_2 dimers after 50 ps pump-probe timedelay that seems to reach a plateau at 200 ps. Also with indium the ejection startet at 50 ps but had a steeper rise [5]. Further scans at higher delays have to be conducted to ensure that this is already a plateau. The exponential fit of the dimer ejection, that is measured as an ion yield after photo ionization, gives the following behaviour:

$$\text{Ion yield(t)} = (\text{-101.4*exp(-t/76.9 ps)} + 91.9) \text{ counts}$$
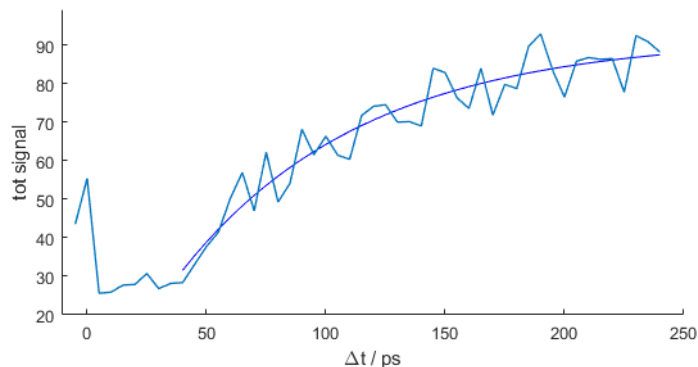
Figure 61: Mass timescan of the dimer ejection that displays a rise in mass 54 and thereby a rise in Al_2 dimers after 50 ps pump-probe timedelay. The signal seems to reach a plateau at 200 ps but frther scans at higher delays have to be conducted to confirm the time of a reached plateau. This signal has been retrieved without subtracting pump and probe signals. (Lab.book: 07.04.2021)

For the time period in which the excited molecules are within the droplet, the He_N interaction is expected to reduce the oscillation contrast and lead to decoherence and dissipation. After 200 ps 90 percent of Al_2 dimers seem to have left the droplets.

Without the He_N environment the oscillation should be unperturbed and thereby the oscillation strength for higher pump-probe delays should stay constant. Within figure 47 the oscillation amplitudes in the time domain are shown for three timescans. The oscillation amplitude seems to staying constant after 111 ps. The courses of the evaluation in frequency domain show the same trend, although the oscillation contrast is very low already, making it difficult to prove the assumption of oscillation conservation outside the He_N with Fourier transformation and sinusoidal fits. For this, further PE timescans with better resolution are needed.

3.3 Al_2 State Assignment for Observed Dynamics

The vibronic constants of the Al_2 band systems can be found in reference [12] and have been used to calculate revival times and oscillation periods that can be found in table 3. The measured and theoretical values have been compared in table 4. The E-state is most likely to be observed and also the F state has characteristics that are similar to our measurements. Like stated in section 1.2.4, the E' state would be the most intense band, but due to non-adiabatic coupling a fast dissociation makes it not practical for microsolvation.

The fundamental frequencies of the E_0-state and E_1-state in gas phase are (5.98 ± 0.03) THz and (5.99 ± 0.03) THz for the oscillation frequency and they have a revival time τ_{rev} of $(33.1$ ps $\pm 0.3)$ ps and (30.9 ± 0.3) ps respectively. The measured values range from (5.62 ± 0.08) to

(5.8 ± 0.13) THz, with 315 nm and 319.5 nm, in the frequency domain with SWFTs and from (5.81 ± 0.02) THz to 5.83 THz, for 319.4 nm and 319.5 nm, with sinusoidal fits in the time domain. Since the influence of helium is expected to squezze the potential energy curves and thereby increase the oscillation period, we would have expected a higher but not lower oscillation frequency than in gas phase.

The revival times of the F-state span from 27.8 ps to 29 ps which is not overlapping with the measured period. The oscillation frequencies of this state are within 6.3 and 6.6 THz and there is less agreement than with the gas phase literature values of the E-state.

The E-state is shown to reach from 344 nm to 366 nm in gas phase. With a shift of 36 (± 15) nm due to the helium interaction, that can be deduced from the helium bubble expansion, this would correspond to an excitation wavelength range in the helium bath from 308 nm to 330 nm. With excitation pulses between 315 nm and 319 nm we have excited the center of the E-state. The high uncertainty stems from the fact that the ionic state is shifted in the other direction due to the helium and thereby increasing the bubble expansion. Therefore the energy shift of the E-state is in fact smaller than the measured bubble expansion.

To summarize, the E-state is the most likely candidate for the observed dynamics, although the oscillation frequency is lower than the measurements in gas phase and should actually be even higher due to the helium influence. Nevertheless, the helium bubble expansion shows an energetic shift that let us expect to excite the E-state and the oscillation frequency and the revival time fit the theoretical values in good approximation.

3.4   Comparison of In_2 to Al_2

There have been conducted successful experiments with In_2 where molecular dynamics could be observed. Figure 62 and figure 63 compare the original oscillation and the first two revivals of aluminium to the measurements of indium. One can see that the PE signal and also the SWFT signal at the half revival of the 345 nm pump signal of indium is lower than at the full revival. This differs from the E-state of aluminium, which has stronger half revival signals.
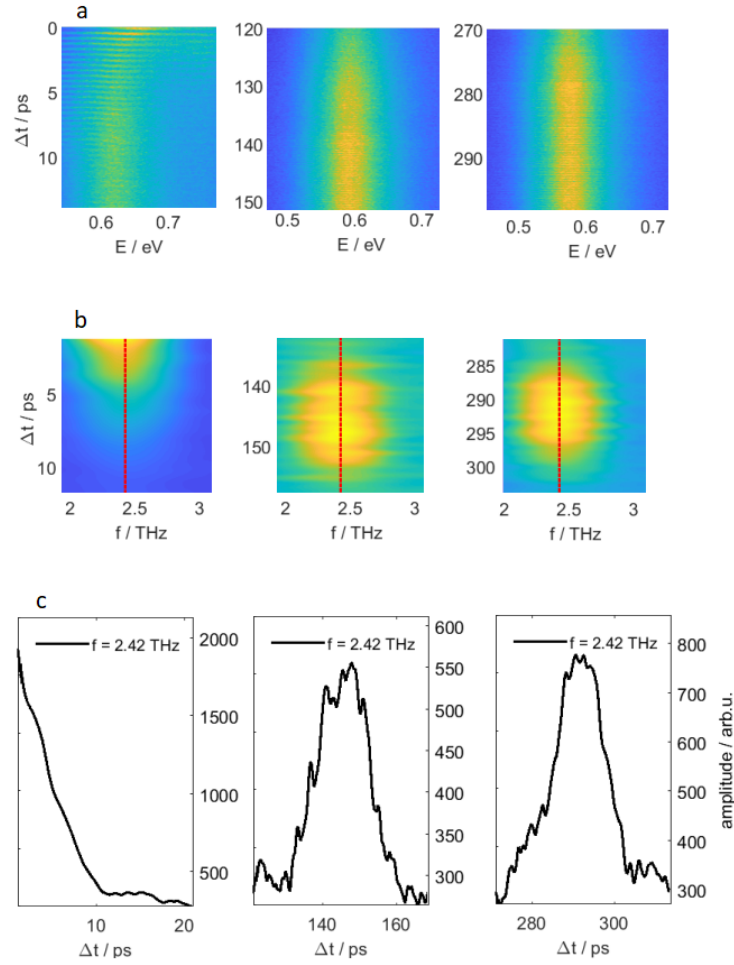
Figure 62: Indium dimer molecular dynamics a.) PE timescans at the original oscillation and the first two revivals b.) SWFTs of the transient PE spectra with 345 nm pump pulse c.) Cut through the spectrograms at 2.42 THz (Lab.book: 18.04.2018)
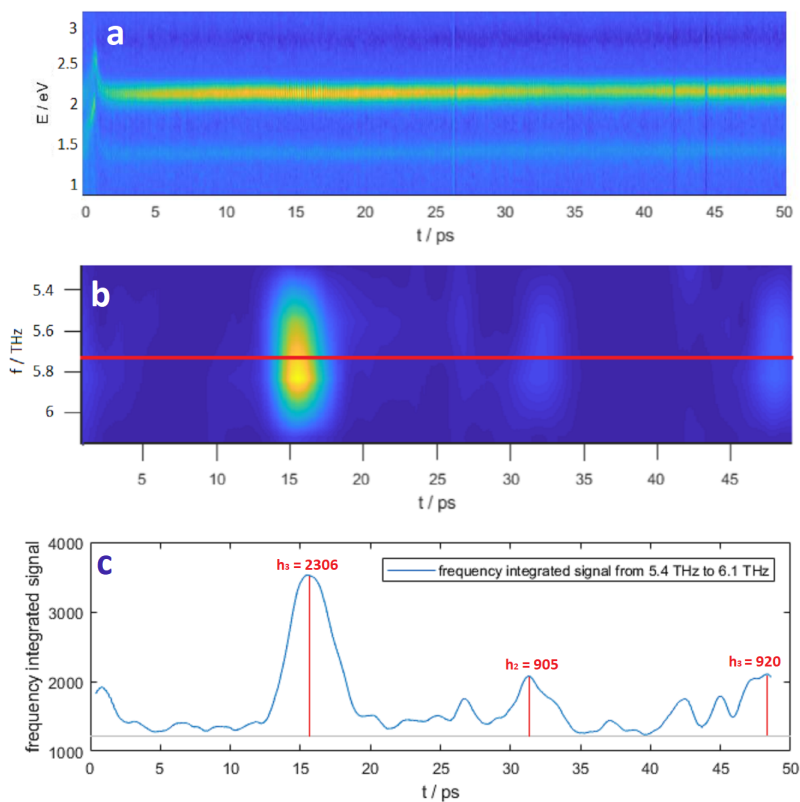
Figure 63: Aluminium dimer molecular dynamics a.) PE timescans at the original oscillation and the first two revivals with 319.5 nm pump pulse b.) SWFTs of the transient PE spectra c.) Integrated spectrogram between 5.4 and 6.1 THz (Lab.book: 01.12.2020)

Due to the four times higher mass of indium the oscillation frequency is lower. The revival time of aluminium is 1/10th of the revival time of indium what is very favourable for microsolvation. Table 5 shows the differences between the evaluated In_2 state with 345 nm pump pulse and the suspected E-state of Al_2.

Table 5: Comparison between the observed states of aluminium and indium dimers. ν... Frequency of wavepacket oscillation; τ_{rev} ... revival time; p_{He}... Pressure Helium; T_{nozzle} ... Nozzle temperature; I_{PU} ... Pickup current; $U_{Repeller}$ ... repeller voltage; wl_{pump} ... Pump wavelength; P_{pump} ... Pump power; wl_{probe} ... Probe wavelegth; P_{probe} ... Probe power

Parameter	Unit	Al_2 (Lab.book 01.12.2020)	In_2 (Lab.book 21.05.2021)
Crucible setup	-	$Al_2 O_3$	$Al_2 O_3$
ν	THz	5.73 ± 0.13	2.42 ± 0.05
τ_{rev}	ps	15.7 ± 0.2	142 ± 9
T_{nozzle}	K	11.3	15
I_{PU}	A	51	43
Further settings	-	THG, Second PUC-oven	1 mm BBO crystal
$U_{Repeller}$	V	-0.3	+0.9
wl_{pump}	nm	319.5	345
P_{pump}	mW	35	2.7
wl_{probe}	nm	269.6	406
P_{probe}	mW	2	13

3.5   Next Steps within the Project "Photoinduced Dynamics in a Quantum Fluid Environment"

This should be the next steps in the examination of aluminium dimers:

1. Find a suitable crucible setup that is resistant enough to enable a measuring period of at least two weeks. Therefore the BN coating of the tungsten wires could be considered. Additionally a new form of radiation shield could be installed to reduce the required heating current.

2. A scan over the whole stage will reveal the exact position of each revival. It will be possible to determine the frequency and maximal oscillation amplitude of each revival and the rising and falling of the Fourier transformed signal to measure the dispersion time without further dopants.

3. After a successful scan, further dopants should be included in a controlled way and the effects on the oscillation frequencies, amplitudes, dispersion time and revival periods evaluated.

4. An ion scan at higher time delays should be conducted to determine the time at which a plateau in the dimer ejection is reached. Ideally, a first scan from -25 ps - 275 ps and a second scan from 250 ps - 550 ps should be conducted.

This should enable the determination of the revival times, dispersion times, oscillation frequencies and amplitudes with and without further dopants and should tell us the interaction time

of the aluminium dimers with further dopants until the ejection from the He_N. Thereby the influence of additional dopants on the molecular dynamics should be assessable.

4 Discussion and Outlook

Aluminium has been investigated with femtosecond spectroscopy to examine its usability within the generation of a controlled microsolvation environment. While providing favourable conditions for microsolvation investigations by offering short revival periods, aluminium has the drawback of its high reactivity. A very stable state with a revival period of (15.8 ± 0.2) ps has been investigated. This revival period is $1/10^{\text{th}}$ of the revival time of the before investigated indium dimer. This is a very valuable feature, since the long revival period was the reason that indium could not be used for microsolvation. With the short revival times of the found molecular dynamic of aluminium dimers, the influences of additional dopants can be traced.

The found dynamics can be ascribed, most likely, to the E state. In gas phase this should be a very stable state and the revival times lie between 29 ps up to 33 ps. This makes the first measured revival at (15.5 ± 0.5) ps a potential half revival. The mean oscillation frequency of (5.81 ± 0.02) THz was obtained in the time domain analysis with a higher precision then in the frequency domain. The measured PE-energy before the bubble expansion is 2.58 eV and after the bubble expansion it is 2.18 eV. An excitation from the $X^3\Pi_{\text{u}}$ ground state and ionization to the lowest dipole connected ionized state $A^2\Pi_{\text{u}}$ would give a PE energy of 2 eV. Since the PECs of the ground state and excited state have higher energies and the ionized state is at lower energies within the helium environment, the additional 0.18 eV are likely to stem from a residual effect of the helium environment after the bubble expansion. A second weaker signal with 0.77 eV less energy, that shows the exact same bubble expansion, oscillation pattern and revival times, is not yet explainable.

Within the measurements so far, the oscillation resolution drops very fast. After seven revivals the amplitude of the oscillation in the frequency domain is close to the mean amplitude. In the time domain most of the oscillations can be fitted what speaks for a remaining constant oscillation after 111 ps. The measurement of the dimere ejection shows that 75 percent of the dimers have been ejected at this time delay. Nevertheless, further scans should be conducted and better measurement conditions should make clear if the oscillation contrast stays constant after 111 ps. In further measurements, a scan over the whole stage should enable us to observe the rising and falling of the revival signals. After ejection, the missing helium environment can also influence the revival periods and thus the measurement windows might not have been at the right time delays. Hence, a full scan over the stage will show the influence of dimer ejections on dephasing and help to investigate, if after the dimer ejection, the oscillation strength stays constant.

In indium, a helium bubble oscillation with a period of 30 ps has been observed. Our mea-

surements provide further observations that speak for a similar dynamic with aluminium dimers.

While with indium the original WP dynamic had the highest amplitude and the half revival was weaker than the first full revival, with aluminium the half revival gives a stronger signal than the original oscillation and the first full revival. This observation could be due to the bubble oscillation but is not yet explainable.

Throughout this thesis, the oven crucible setting had to be changed and altered several times. The high reactivity of aluminum lead to reactions with the previously used Al_2O_3 crucibles and tungsten and tantalum used for basket holders and shielding. The new BN crucibles are better suited for fast heating and the evaporation of aluminium. One of the next challenges lies in finding a way to prevent the aluminium from alloying and reacting with the tungsten basket holders to elongate the measurement periods.

As soon as a reliable crucible setup is found, further steps towards microsolvation can be conducted. The combination with other atoms and solvents will give further insights into the dependence of wavepacket dephasing and energy dissipation on the presence of mediator species. Working towards the generation of controlled microsolvation environments inside He_N, and thereby providing the possibility to examine chemical processes on a femtosecond timescale, will be a valuable contribution to Physical Chemistry.

List of Figures

List of Tables

References

[1] J. Peter Toennies and Andrey F. Vilesov. Superfluid Helium Droplets: A Uniquely Cold Nanomatrix for Molecules and Molecular Complexes. *Angewandte Chemie International Edition*, 43(20):2622–2648, 2004.

[2] M. Mudrich and F. Stienkemeier. Photoionisaton of pure and doped helium nanodroplets. *International Reviews in Physical Chemistry*, 33(3):301–339, 2014.

[3] H. Schmidt, J. von Vangerow, F. Stienkemeier, A. S. Bogomolov, A. V. Baklanov, D. M. Reich, W. Skomorowski, C. P. Koch, and M. Mudrich. Predissociation dynamics of lithium iodide. *The Journal of Chemical Physics*, 142(4):044303, January 2015. arXiv: 1501.03327.

[4] Bernhard Thaler, Miriam Meyer, Pascal Heim, and Markus Koch. Long-Lived Nuclear Coherences inside Helium Nanodroplets. *Physical Review Letters*, 124(11):115301, mar 2020.

[5] Bernhard Thaler, Pascal Heim, Leonhard Treiber, and Markus Koch. Ultrafast photoinduced dynamics of single atoms solvated inside helium nanodroplets. *The Journal of Chemical Physics*, 152(1):014307, 1 2020.

[6] Bernhard Thaler, Sascha Ranftl, Pascal Heim, Stefan Cesnik, Leonhard Treiber, Ralf Meyer, Andreas W. Hauser, Wolfgang E. Ernst, and Markus Koch. Femtosecond photoexcitation dynamics inside a quantum solvent. *Nature Communications*, 9(1):4006, October 2018.

[7] Miriam Meyer, Bernhard Thaler, Pascal Heim, and Markus Koch. Femtosecond solvation dynamics of indium dimers inside superfluid helium nanodroplets. In *UP2018 - Proceedings*, volume 205. EPJ Web of Conferences, apr 2019.

[8] Anna Gutberlet, Gerhard Schwaab, Özgür Birer, Marco Masia, Anna Kaczmarek, Harald Forbert, Martina Havenith, and Dominik Marx. Aggregation-induced dissociation of $HCl(H_2O)$ below 1 K: The smallest droplet of acid. *Science*, 324(5934):1545–1548, 2009.

[9] H. Haken and H.C. Wolf. *Molekülphysik und Quantenchemie: Einführung in Die Experimentellen und Theoretischen Grundlagen.* Physics and astronomy online library. Springer, 2002.

[10] Robert G. Mortimer. *Physical Chemistry.* Academic Press, 2008.

[11] Lutz Zülicke. *Molekulare Theoretische Chemie: Eine Einführung.* Springer, 2015.

[12] Zhenwen Fu, George W. Lemire, Gregory A. Bishea, and Michael D. Morse. Spectroscopy and electronic structure of jet-cooled Al_2. *The Journal of Chemical Physics*, 93(12):8420–8441, December 1990.

[13] Theoretical study of the spectroscopy of $Al_2{}^+$. *Chemical Physics*, 151(1):1–9, 1991.

[14] M. Meyer. Nuclear wave packet dynamics of indium dimers inside superfluid helium nanodroplets. Master's thesis, TU Graz, 2018.

[15] Bernhard Thaler. *Ultrafast Photoinduced Dynamics of Atoms and Dimer Molecules inside Helium Nanodroplets.* PhD thesis, TU Graz, 2020.

[16] Markus Gühr. *Coherent dynamics of small molecules in rare gas crystals.* PhD thesis, Freie Universität Berlin, 2005.

[17] I. Fischer, M. J. Vrakking, Villeneuve, and D. Stolow. Femtosecond time-resolved zero kinetic energy photoelectron and photoionization spectroscopy studies of I_2 wavepacket dynamics. *Chem. Phys.*, 207:331–354, 1996.

[18] M. Gühr, M. Bargheer, M. Fushitani, T. Kiljunen, and N. Schwentner. Ultrafast dynamics of halogens in rare gas solids. *Physical Chemistry Chemical Physics*, 9:779–801, 2007.

[19] C. Lienau and A. H. Zewail. Solvation ultrafast dynamics of reactions, dissociation and caging dynamics in the gas-to-liquid transition region. *The Journal of Physical Chemistry*, 100:18629–18649, 1996.

[20] R. Monni, G. Auböck, D. Kinschel, K. M. Aziz-Lange, H. B. Gray, A. Vlcek, and M. Chergui. "conservation of vibrational coherence in ultrafast electronic relaxation: The case of diplatinum complexes in solution. *Chemical Physics Letters*, 683:112–120, 2017.

[21] R. Zadoyan, M. Sterling, and V. Apkarian. Dynamical spectroscopy of many-body interactions. coherent vibrations and predissociation of I_2 (b) in solid kr. " *Journal of the Chemical Society, Faraday Transactions*, 92:1821–1829, 1996.

[22] M. Mudrich, P. Heister, T. Hippler, C. Giese, O. Dulieu, and F. Stienkemeier. High-resolution spectroscopy of triplet states of Rb2 by femtosecond pump-probe photoionization of doped helium nanodroplets. *Phys.Rev.*, 80(4):042512, October 2009. arXiv: 0907.2774.

[23] M. Schlesinger, M. Mudrich, F. Stienkemeier, and W. T. Strunz. Dissipative vibrational wave packet dynamics of alkali dimers attached to helium nanodroplets. *Chemical Physics Letters*, 490:245–248, 2010.

[24] Bernhard Thaler, Miriam Meyer, Pascal Heim, and Markus Koch. Long-lived nuclear coherences inside helium nanodroplets. *Physical Review Letters*, 124:115301, 03 2020.

[25] C. Callegari and W. Ernst. *Helium Droplets as Nanocryostats for Molecular Spectroscopy—from the Vacuum Ultraviolet to the Microwave Regime*, volume 3, pages 1551–1594. John Wiley Sons, 1 edition, 2011.

[26] Vapor pressures of the chemical elements. `https://www.powerstream.com/vapor-pressure.htm`. Accessed: 2020-11-10.

[27] Rein Munter, Anatoli Parshin, Leonid Yamshchikov, Vladimir Plotnikov, Valeri Gorkunov, and Viktor Kober. Reduction of tantalum pentoxide with aluminium and calcium: Thermodynamic modelling and scale skilled tests. *Proceedings of the Estonian Academy of Sciences*, 59:243–252, 01 2010.

[28] Material deposition chart. `https://www.lesker.com/newweb/deposition_materials/materialdepositionchart.cfm?pgid=0`. Accessed: 2021-06-24.

[29] Jr. Bauschlicher, Charles W., Leslie A. Barnes, and Peter R. Taylor. The lowest ionization potentials of al2. *Journal of Physical Chemistry*, (19890001234), January 1988.

[30] A. Kautsch, M. Koch, and W. E. Ernst. Photoinduced molecular dissociation and photoinduced recombination mediated by superfluid helium nanodroplets. *Phys. Chem.*, 17:12310–12316, 2015.

[31] Andreas Braun and Marcel Drabbels. Imaging the translational dynamics of CF3 in liquid helium droplets. *Physical Review Letters*, 93(25):253401, December 2004.